



저작자표시-비영리-변경금지 2.0 대한민국

이용자는 아래의 조건을 따르는 경우에 한하여 자유롭게

- 이 저작물을 복제, 배포, 전송, 전시, 공연 및 방송할 수 있습니다.

다음과 같은 조건을 따라야 합니다:



저작자표시. 귀하는 원저작자를 표시하여야 합니다.



비영리. 귀하는 이 저작물을 영리 목적으로 이용할 수 없습니다.



변경금지. 귀하는 이 저작물을 개작, 변형 또는 가공할 수 없습니다.

- 귀하는, 이 저작물의 재이용이나 배포의 경우, 이 저작물에 적용된 이용허락조건을 명확하게 나타내어야 합니다.
- 저작권자로부터 별도의 허가를 받으면 이러한 조건들은 적용되지 않습니다.

저작권법에 따른 이용자의 권리는 위의 내용에 의하여 영향을 받지 않습니다.

이것은 [이용허락규약\(Legal Code\)](#)을 이해하기 쉽게 요약한 것입니다.

[Disclaimer](#)

공학박사 학위논문

**Computational identification of p-type
transparent semiconductors**

계산과학을 통한 p형 투명 반도체 탐색 연구

2018년 8월

서울대학교 대학원

재료공학부

윤 용

Abstract

Computational identification of p-type transparent semiconductors

Yong Youn

Materials Science and Engineering

The Graduate School

Seoul National University

Transparent oxide semiconductors have been used in various applications such as display and solar cell panels. The development of n-type oxides such as In_2O_3 and ITO realized the transparent electronics. In order to fabricate highly efficient transparent electronic devices, high performance p-type transparent oxide semiconductors comparable to the n-type oxides are required. However, the performance of present p-type oxides is much inferior to that of n-type oxides in spite of enormous efforts. Recently, several novel p-type candidates are suggested by using high-throughput approach with the density functional theory calculations. However, candidate materials have not been verified in experiment, which implies the necessity of a reliable theoretical descriptor.

In this dissertation, we propose a reliable and computationally efficient descriptor for p-type dopability using the formation energy of hydrogen interstitial defect. The predictive power of hydrogen descriptor is demonstrated by showing that the hydrogen descriptor

can distinguish well known p-type and n-type oxides. Using the hydrogen descriptor, we conduct high-throughput screening for most binary oxides and selected ternary oxides including Sn^{2+} - and Cu^{1+} -bearing oxides as well as oxychalcogenides. As a result, we introduce $\text{La}_2\text{O}_2\text{Te}$ and CuLiO as promising p-type candidates, which are validated through the full intrinsic defect calculations. Additionally, we identify simple descriptors that correlate with hydrogen descriptor. By using the simple descriptors in the multi-step high-throughput screening, we screen most oxide compounds (~17,000 oxides) in Aflow database. As a result, we suggest new p-type candidates such as Na_2PtO_2 , $\text{La}_2\text{O}_2\text{S}_2$ and $\text{La}_2\text{SiO}_4\text{Se}$.

Keywords: density functional theory, high-throughput screening, p-type transparent semiconducting oxides

Student Number: 2014-30231

Contents

Abstract
Contents
List of table and figures
1. Introduction 1
1.1. Overview of transparent semiconductors 1
1.2. p-type transparent semiconducting oxides (TSOs) 3
1.3. High-throughput screening for p-type TSOs 6
1.4. Goal of the dissertation 8
1.5. Organization of the dissertation 9
2. Theoretical background 10
2.1. Density functional theory (DFT) 10
2.1.1 Hohenberg and Kohn theorem 10
2.1.2 Kohn-Sham equation 12
2.1.3 Exchange-correlation energy 14
2.2. Beyond DFT 15
2.2.1 DFT+ U 15
2.2.2 Hybrid functional 16
2.3. Defect calculations 18
2.3.1 Defect formation energy 18
2.3.2 Cell-size corrections for supercell approach 19
3. Hydrogen descriptor for p-type screening 22

3.1. Introduction	22
3.2. Computational methods	24
3.2.1. Density functional theory	24
3.2.2. Band gap	25
3.2.3. Effective mass	28
3.2.4. Branch-point energy	34
3.3. Hydrogen descriptor	36
3.3.1. Limitation of previous descriptor	36
3.3.2. Defect formation energies of known semiconducting oxides	40
3.3.3. Hydrogen descriptor for p-type oxide screening	44
3.3.4. Automatic procedure for hydrogen descriptor	51
3.4. High-throughput screening of p-type oxides	56
3.4.1. Screening over binary oxides	56
3.4.2. Screening over ternary oxides	58
3.4.3. Defect formation energy for candidates	62
3.5. Summary	68
4. High-throughput screening of p-type oxides using material database	69
4.1. Introduction	69
4.2. Computational methods	71
4.2.1. Density functional theory	71
4.2.2. Candidate descriptors for p-type oxides	72
4.2.3. Pearson correlation coefficient	73
4.2.4. Receiver operating characteristic curve	75

4.3. Computational methods	71
4.3.1. Simplified descriptor for p-type oxides	77
4.3.2. Screening over the oxides in the AFLOW database	84
4.3.3. Promising candidates	93
4.4. Summary	105
5. Conclusion	106
Bibliography	108
국문초록	113

List of table and figures

Table 1.1. Properties of p-type transparent conducting oxides	4
Table 3.1. List of p-type candidate oxides	61
Table 4.1. Four conditions from binary classifier	76
Table 4.2. List of p-type candidate TSOs	88
Figure 3.1. Comparison of band gap	3
Figure 3.2. Constant energy surface for MgO	29
Figure 3.3. Cut-off for effective mass	31
Figure 3.4. Comparison of band structure	33
Figure 3.5. Branch point energy of MgO	35
Figure 3.6. Validation of the known descriptors	37
Figure 3.7. Defect formation energies of insulating oxides	39
Figure 3.8. Defect formation energies of p-type oxides	41
Figure 3.9. Defect formation energies of n-type oxides	43
Figure 3.10. Description for FEH	45
Figure 3.11. Validation of FEH	47
Figure 3.12. FEH versus ionization potential	48
Figure 3.13. FEH versus H(+/-) level	50
Figure 3.14. Schematic work flow to estimate FEH	54
Figure 3.15. VBM correction for FEH	55
Figure 3.16. Binary p-type candidates	57
Figure 3.17. Ternary p-type candidates	60
Figure 3.18. Properties of CuLiO	63
Figure 3.19. Properties of SnSO ₄	65

Figure 3.20. Properties of $\text{La}_2\text{O}_2\text{Te}$	67
Figure 4.1. The examples of Pearson correlation coefficient	74
Figure 4.2. Pearson correlation coefficient of various factors	79
Figure 4.3. Comparison of FEH with simple descriptors	81
Figure 4.4. ROC curve for the w_{O} and $E_{\text{g,HSE}}$	83
Figure 4.5. Screening procedure for p-type TSOs	86
Figure 4.6. Comparison of band gap	87
Figure 4.7. p-type TSO candidates	92
Figure 4.8. Splitting diagram of the d orbital electrons	94
Figure 4.9. Properties of Na_2PtO_2	97
Figure 4.10. Properties of $\text{La}_2\text{O}_2\text{S}_2$	99
Figure 4.11. Properties of $\text{La}_2\text{SiO}_4\text{Se}$	101
Figure 4.12. Properties of Sr_3BPO_3	103
Figure 4.13. Properties of Ba_3BPO_3	104

1.1 Overview of transparent semiconductors

Transparent semiconducting materials are used in various applications such as solar cell, display panel and light emitting diodes due to their unique properties that electrically semiconducting and transparent to visible light.^[1-3] Inherently, transparent materials with wide band gap are electrically insulating. However, intrinsic defects or extrinsic dopant allow the conducting and transparent materials for the transparent electronic devices. Especially, transparent semiconducting oxides has been received much attention to replace the conventional silicon based semiconductor. The development of transparent semiconducting materials was begun in n-type oxides such as SnO₂^[4] and ZnO^[5]. In 2003, Nomura *et al.* reported the fabrication of oxide thin film transistor (TFT) using single crystalline InGaO₃(ZnO)₅ (sc-IGZO) single-crystalline semiconductor layer.^[6] Prior to the discovery of sc-IGZO, the performance of oxide TFTs was not promising to replace the conventional Si based TFT though there had been the attempts to utilize the oxide TFT in the devices.^[7,8] However, the appearance of high performance material, sc-IGZO, proves that the oxide TFTs can be realized. In the next year, TFT using amorphous InGaZnO (a-IGZO) was proposed.^[9] The outstanding advantage of the TFT with amorphous phase is that it is possible to

deposit the homogeneous thin films on wide area at low temperature with low cost. The TFT with a-IGZO was deposited at the too high temperature and exhibited high electron mobility (over $10 \text{ cm}^2/\text{Vs}$) exceeding hydrogenated amorphous silicon ($\sim 1 \text{ cm}^2/\text{Vs}$)^[10]. The success of n-type oxide TFT has attracted interest in p-type oxides for ambipolar devices. However, p-type oxides still suffer from their poor performance in the electrical conductivity or transparency.

1.2 p-type transparent semiconducting oxides (TSOs)

In the recent past, various n-type transparent semiconducting oxides such as ITO and In_2O_3 were discovered and successfully commercialized in optoelectronic devices due to their good device performance, good conductivity and transparency.^[7,8] However, there are only a few p-type oxides and their performance are considerably inferior to the n-type counterpart in spite of tremendous efforts to discover them. The most widely known p-type transparent oxide is delafossite CuAlO_2 discovered by H. Hosono's research team in 1997 which has a wide band gap over 3.1 eV and p-type conductivity.^[11] Since p-type conductivity was demonstrated for CuAlO_2 , various studies revealed a series of p-type TOSs with Cu or Ag based delafossite structures such as $\text{CuM}^{\text{III}}\text{O}_2$, $\text{AgM}^{\text{III}}\text{O}_2$ ($\text{M}^{\text{III}}=\text{Sc, Cr, Co, Ga, In}$), as well as SrCu_2O_2 , LaCuOSe , and Rh_2ZnO_4 .^[12-18] Table 1 shows the performances of known p-type TSOs.^[19] However, none of them has high conductivity and excellent transparency at the same time as shown in Table 1. In the case of p-type oxides of which hole conductivities are higher than 10 Sm^{-1} , the transparencies are lower than 70%. On the contrary, the p-type oxides with good transparency have hole conductivities below 1 Sm^{-1} . Additionally, well known p-type oxides such as SnO and Cu_2O have stability issues in spite of the appreciable conductivity.^[20,21]

Table 1.1 Conductivity, mobility and transparency of p-type transparent conducting oxides^[19]

Material	Conductivity (S/cm)	Mobility (cm ² /Vs)	Transparency	Reference
NiO	7	~2	Fair	Sato <i>et al.</i> 1993
	0.14		Fair	Ohta <i>et al.</i> 2003
AlCuO ₂	1	10.4	Excellent	Kawazoe <i>et al.</i> 1997
	0.3	0.13		Yagani <i>et al.</i> 2000
SrCu ₂ O ₂ :K	0.048	0.46	Excellent	Kudo <i>et al.</i> 1998, Ohta <i>et al.</i> 2002
In ₂ O ₃ -Ag ₂ O	100	17	Poor	Minami <i>et al.</i> 1998
LaCuOS:Sr	0.026		Excellent	Ueda <i>et al.</i> 2000
CuInO ₂ :Ca	0.0028		Excellent	Yagani <i>et al.</i> 2000
CuScO ₂ :O	30	<0.5	Poor	Duan <i>et al.</i> 2000
	25		Poor	Kykyneshi <i>et al.</i> 2004
CuScO ₂ :Mg	0.01		Excellent	Kykyneshi <i>et al.</i> 2004
CuGaO ₂	0.063	0.23	Excellent	Ueda <i>et al.</i> 2001
CuGaO ₂ :Ca	0.3-1	<0.5	Fair	Jayaraj <i>et al.</i> 2001
CuCrO ₂ :Mg	220	<0.5	Poor	Nagarajan <i>et al.</i> 2001
AgCoO ₂	0.2		Fair	Tate <i>et al.</i> 2002
CuGaO ₂ :Fe	~1		Fair	Tate <i>et al.</i> 2002
CuYOSr ₂ :Cu ₂ Zn	0.12		$E_g = 2.6$ eV	Hirose <i>et al.</i> 2002
O ₂ S ₂ :Na				
BaCu ₂ S ₂	17	3.5	$E_g = \sim 2.3$ eV	Park <i>et al.</i> 2002
CuNi _{0.67} Sb _{0.33}	0.05		Fair	Nagarajan <i>et al.</i> 2002
O ₂ :Sn				
LaCuOSe	24	8	$E_g = 2.8$ eV	Hiramatsu <i>et al.</i> 2003
LaCuOSe:Mg	140	4	$E_g = 2.8$ eV	Hiramatsu <i>et al.</i> 2003
ZnRh ₂ O ₄	0.7		$E_g = 2.1$ eV	Mizoguchi <i>et al.</i> 2003

The scarcity of p-type transparent oxides results from the fundamental properties of oxides. One is low valence bands level of oxides. Therefore, holes are easily compensated by donor like defects such as oxygen vacancy and ubiquitous hydrogen, which leads to the low hole concentration. Another character is that the valence-band maximum (VBM) mainly consists of localized oxygen 2p orbitals resulting in a large hole effective mass (m_h). Because of such fundamental restrictions, it is difficult to find new p-type oxides in restricted searching space. Thus, high-throughput screening base on the computational method should be performed.

1.3 High-throughput screening for p-type TSOs

Recently, it is possible to select the counter material through first principle calculation with the improvement of computational performance and the establishment of the density functional theory (DFT) calculation method with high accuracy. Using the method, several studies have been conducted to search new p-type semiconducting oxides that surpass the limitation of known p-type oxides.^[22-25] G. Hautier *et al.* estimated the p-type performance using band gap and hole effective mass.^[22] Transparency can be directly assessed by the optical band gap (E_g^{opt}) in DFT calculations. Whereas, to evaluate the p-type conductivity, several physical properties should be considered including carrier density, scattering time, and effective mass, even within the simple Drude model. In the previous study, however, only m_h is used as a primary descriptor for p-type conductivity because it is difficult to estimate the other parameters. Using the descriptors, they suggested several candidates, and then they calculate the defect formation energy for the selected materials to evaluate hole dopability. Sarmadian *et al.* added the branch point energy (BPE) to the primary descriptor together with band gap and m_h to consider the dopability.^[24] In the complex band structure, BPE constitutes a universal quantity corresponding to a charge neutrality level and it is thought to show the conduction character. For example, BPE close to the valence edge may result in high hole dopability. The BPE and m_h are suitable parameters for high-throughput screening

since they can be easily obtained from the DFT calculations on primitive cells. However, none of suggested materials using them is verified in experiment, which implies that they are insufficient to search p-type oxides and we need more promising descriptors.

1.4 Goal of the dissertation

In this dissertation, we perform the high-throughput screening based on the density functional theory to discover new p-type oxides. First, we identify a promising descriptor to distinguish p-type oxides by studying the band gap, hole effective mass and defect chemistry of the well-known p-type and n-type oxides.^[26] We verify that the suggested descriptor, hydrogen descriptor, is promising and reliable to find p-type oxides. Then, we screen new promising p-type candidates with good transparency and good electric conductivity using the hydrogen descriptor. Second, we extend the screening space to all oxides reported in the material database. To realize the high-throughput screening, we search new descriptors which are effective, practical and low computational cost by estimating the correlation with hydrogen descriptor. Using low cost descriptors, we perform the screening procedure and rapidly identify the p-type candidates. Then, we conduct more accurate but more expensive calculation for remaining compounds. Through the high-throughput screening procedure, we identify new p-type candidates which have not been reported. Additionally, we estimate the intrinsic and hydrogen related defect formation energy calculation to figure out the source of holes.

1.5 Organization of the dissertation

This dissertation consists of five chapters. Chapter 1 is the introduction of this study. In chapter 2, we present the theoretical backgrounds of density functional theory and the basic method used in this study. In chapter 3, we propose a novel descriptor for p-type oxides and identify several p-type candidates from high-throughput screening for binary and limited ternary oxides. In chapter 4, we perform the multi-step high-throughput screening for most of oxides and suggest unreported p-type candidates. Finally, in chapter 5, we summarize the overall results of each chapter.

2.1 Density functional theory (DFT)

2.1.1 Hohenberg and Kohn theorem

First-principles calculation is a computational method based on the quantum mechanics, which does not require any empirical parameter obtained from experiment. However, it is a hard problem to calculate many-electrons quantum mechanical behavior. Thus, we use approximation schemes called as density functional theory (DFT).

DFT is based on the Hohenberg-Kohn theorem introduced in 1964.^[27] The essential point of this theorem is that a functional of ground state charge density $\rho(r)$ is necessary and sufficient condition to determine the electronic structure and the energy of the system. We are able to calculate charge density and wave function solving the Schrödinger equation. The total energy E of the system is given by the following equation:

$$E[\rho] = F[\rho] + \int \rho(r) V_{\text{ext}}(r) dr \quad (2.1)$$

with

$$F[\rho] = T[\rho] + U_{\text{ee}}[\rho] \quad (2.2)$$

where F is the universal functional, V_{ext} is the external potential, T is kinetic energy and U_{ee} is electron-electron interaction energy. According to the variational principles, it can be proven that the total energy in Eq. (2.1) is minimum when $\rho(r)$ corresponds to the true

ground state charge density. However, the theorem is not sufficient to solve the electronic structures of many-body systems.

2.1.2 Kohn-Sham equation

The Hohenberg and Kohn theorem provides practically unsolvable Schrödinger equation with extremely high degree of freedom. In 1965, Kohn and Sham theorem were suggested to solve the many-body system.^[28] In the system, electrons interact with other electrons, which is too complicated to solve. Thus, we consider the other electrons as effective potential and simplify the system. The effective potential consists of three parts:

$$V_{\text{eff}}(r) = V_{\text{ion}-e} + V_{e-e} + V_{xc} \quad (2.3)$$

$V_{\text{ion}-e}$ is the ion-electron interaction energy (Ewald energy), V_{e-e} is the electron-electron coulomb interaction energy (Hartree energy) and V_{xc} is the exchange-correlation potential which is related to many body system. As we introduce the effective potential, the Schrödinger equation becomes simple one particle equation.

$$\left[-\frac{\hbar^2}{2m} \nabla^2 + V_{\text{eff}}(\rho(\vec{r})) \right] \psi_i(\vec{r}) = \epsilon_i \psi_i(\vec{r}) \quad (2.4)$$

Eq. (2.4) is the Kohn-Sham Hamiltonian established with effective potential. It consists of kinetic energy term and effective potential term. Using the equation with trial charge density and wave vectors from atomic potential of the system, we estimate the effective potential. Since many-body interaction terms are only included in effective potential, we can solve the Schrödinger equation reduced to single electron problem by the variational principles. Next, we calculate the fermi energy and new charge density. Until the difference between given charge density and obtained charge density is smaller than given criteria, this self-consistent calculation is

repeatedly performed. Through the process, we can obtain the optimized charge density and wave function.

2.1.3 Exchange-correlation energy

In the DFT theorem, we imply the exchange-correlation potential to simplify the many-body system. One of the method is local density approximation (LDA). LDA was suggested by Kohn and Sham.^[28] It assumed that the exchange-correlation energy of the system is identical to that of the homogeneous electron gas that has same local density. Thus, the exchange-correlation potential just depend on the local density of the system.

$$E_{xc}^{LDA}[\rho(r)] = \int \epsilon_{xc}^{LDA}(\rho(r))\rho(r)dr \quad (2.5)$$

The LDA is suitable for calculating the systems that have smooth electron density such as the free electron like model. However, it is not adequate for using the systems that have rapidly changing electron density such as the transition metal.

In order to overcome the problem, generalized gradient approximation (GGA) was introduced by Perdew^[29] and Becke^[30]. In the GGA, not only electron density of local point but also gradient of electron density of local point are considered.

$$E_{xc}^{GGA}[\rho(r), \nabla\rho(r)] = \int \epsilon_{xc}^{GGA}(\rho(r), |\nabla\rho(r)|)\rho(r)dr \quad (2.6)$$

Among the GGA scheme, we use PBE functional which is developed by Perdew, Burke, and Ernzerhof.^[31]

2.2 Beyond DFT

2.2.1 DFT+ U

In the LDA and GGA scheme, the strong on-site Coulomb interaction of localized electrons is not correctly described. DFT+ U is one of the approximation method to enhance the accuracy of DFT calculations for strongly correlated system which contains d , f electrons with an on-site Coulomb interaction U (Hubbard-like term).^[32] The parameter U can be estimated by self-consistent method^[33] and semi-empirical scheme to fit the experimental energetics^[34].

For the reasonable electronic structure, we should apply the DFT+ U scheme for all insulating compounds with localized d and f electrons. However, we apply + U term only for compounds with $3d$ transition metal (V, Cr, Mn, Fe, Co, Ni, Cu, Zn) because the effect of U is negligible when d and f electrons do not build chemical bonding. The U - J values are determined from previous study by L. Wang *et al.*^[34]

2.2.2 Hybrid functional

The conventional DFT schemes such as LDA and GGA successfully describe the various materials properties including structural, mechanical and electronic properties. However, they have a intrinsic limitation that is band gap underestimation due to the omission of self-interaction energy and the absence of discontinuity in a derivative of exchange-correlation energy. The many-body theory such as GW approximation can be a solution to overcome the problems.^[35] However, tremendous computational cost of GW approximation hinders the widespread use of the method.

The hybrid functional can also present more realistic band gap than conventional DFT results.^[36] The exchange correlation functional in the hybrid functional scheme are estimated by mixing the exact exchange from Hartree-Fock (HF) theory and that from conventional DFT. The HF method reduces the self-interaction error in the DFT scheme, which results in the more realistic band gap. In this dissertation, we apply HSE06 method^[37] that is more efficient than PBE0 scheme^[38]. In HF method, the exchange energy is exponentially decaying as a function of distance and we can exclude long-range (LR) part. The exchange energy in HF method requires high computational cost since it is estimated by integrating the orbital directly. Thus, excluding LR part lead to the improvement of computational efficiency. The exchange energy in HSE06 method is defined as

$$E_{xc}^{\text{HSE}} = \alpha E_x^{\text{HF,SR}}(\mu) + (1 - \alpha) E_x^{\text{PBE,SR}}(\mu) + E_x^{\text{PBE,LR}}(\mu) + E_c^{\text{PBE}} \quad (2.7)$$

where α is mixing parameter and μ is the screening parameter, the

criteria for splitting short-range (SR) and LR. We choose 0.25 as α and 0.2 \AA^{-1} as μ .

In the most case, HSE06 calculation shows improved band gap close to the experimental gap. However, it still underestimate band gap of some cases especially high band gap materials. In those cases, we can obtain band gap more close to the experiment by adjusting the mixing parameter.

2.3 Defect calculations

2.3.1 Defect formation energy

In the supercell formalism, defect formation energy of a charged defect can be evaluated by following equation.

$$E_{\text{For}}(\text{defect}, q) = E_{\text{tot}}(\text{defect}, q) - E_{\text{tot}}(\text{perfect}) + \sum N_i \mu_i + q(\varepsilon_F + \varepsilon_{\text{VBM}}) + E_{\text{corr}} \quad (2.8)$$

where q is the charge state, N_i and μ_i are the number and chemical potential of the chemical species i . In Eq. (2.8), ε_F indicates the Fermi energy with respect to the energy at the valence band maximum (ε_{VBM}), and E_{corr} is the correction term for the finite supercell. The chemical potentials reflect the experimental growth condition.^[39,40]

2.3.2 Finite cell-size corrections for supercell approach

The use of periodic boundary conditions has many advantages to estimate the properties of perfect crystal. For the defect calculation, however, this approach can make serious problems due to the finite cell size. When we calculate the defect formation energy, we suppose that the concentration of defects is low and each defect does not interact with another defect. Thus, we should perform the DFT calculation using the infinite cell to estimate the exact defect formation energy but it is impossible. For that reason, we use supercell approach where the cell size is sufficiently large enough to neglect the interactions with the periodic images of defects. For the charged defect calculation, however, it is difficult to make sufficiently large supercell since Coulomb interaction between charged defect is strong and long-range. To overcome the problem, various approaches have been suggested.

Potential alignment correction. In the supercell formalism, the averaged Coulomb potential is fixed to be zero due to the periodic boundary condition.^[41,42] For that reason, there is the shift of VBM, which affects the formation energy of charged defects. Therefore, we need to align the potential level by considering the difference of potential level in the bulk region (far from the defect site) between bulk cell and defected cell. This correction is called potential alignment (PA) correction.

Makov and Payne correction. The supercell formalism has another systematic error due to the limitation of supercell size. In the charged defect system, a charged defect is affected by the periodic images of

defect unless supercell size is large enough to ignore the influence of image charges. Especially, it is difficult to increase the cell-size for influence to be negligible since Coulomb interaction is long range interaction. Therefore, Markov and Payne proposed a correction scheme (MP correction) to complement the finite cell-size error.^[43] The correction in the cubic cell with a length of L is defined as

$$E_{\text{MP}} = \frac{q^2\alpha}{2\epsilon^0 L} + \frac{w\pi qQ}{3\epsilon^0 L^3} + O(L^{-5}), \quad (2.9)$$

where q , α , ϵ^0 and Q are the defect charge (monopole aperiodic charge), Madelung constant, static dielectric constant and second moment of defect charge distribution (quadrupole moment of aperiodic charge), respectively. In Eq. (2.9), the first term indicates the monopole-monopole interaction and the second term represent the monopole-quadrupole interaction. If defect charges are well localized, the correction is physically reasonable. In the real system, however, the charge distribution are complex rather than simply localized at the defect site. Therefore, MP correction sometimes leads to worse result. In addition, it cannot consider anisotropic dielectric behavior of materials.

FNV correction. For the image charge correction, C. Freysoldt and J. Neugebauer and C. G. Van de Walle^[44] proposed self-consistent correction method using planar-averaged electrostatic potential. In this scheme, we can use dielectric tensor and it can extend to non cubic system. Additionally, we do not need to perform the defect calculation for different size of defected cell, which can improve the computational efficiency. Therefore, we used FNV correction with

anisotropic dielectric tensor in this dissertation.^[39]

Band filling correction. Because of supercell calculation, a delocalized (shallow) defect makes dispersive band which is error, and the defect energy states change with the k-points. Therefore, it should be corrected when we use multiple k-points.^[45] However, if single k-point is sampled, band filling correction do not required. Thus, we only use gamma points sampling.

3.1 Introduction

In the recent studies, high-throughput screening based on the density functional theory were conducted to discover new p-type transparent semiconducting oxides (TSOs).^[22-25] Through the screening, they suggested several p-type TSOs considering the band gap for transparency, effective mass for carrier mobility and branch point energy for carrier concentration. However, none of them is verified in experiment until now. Thus, the predictive power of previous descriptors should be explicitly checked. Also, more reliable descriptor should be proposed to find promising p-type candidates.

In this chapter, we propose a novel and promising descriptor for p-type dopability using the formation energy of hydrogen interstitial defect. Prior to introducing hydrogen descriptor, we show the limitation of previous descriptor by estimating the BPE and hole effective mass of well known p-type and n-type oxides. Then, we suggest the hydrogen descriptor by considering the defect formation energy of the oxides of which carrier type is known. Next, we validate the predictive power of the hydrogen descriptor by showing that the hydrogen descriptor can clearly distinguish well known p-type and n-type oxides. In addition, we screen most binary oxides and a selected pool of ternary compounds that covers Sn²⁺- and Cu¹⁺-bearing

oxides as well as oxychalcogenides using the hydrogen descriptor. As a result, we suggest $\text{La}_2\text{O}_2\text{Te}$ and CuLiO as promising p-type oxides.

3.2 Computational methods

3.2.1 Density functional theory

We perform the DFT calculation using Vienna Ab initio Simulation Package (VASP)^[46] with the PBE functional for the exchange correlation energy of electrons.^[31] For *3d* transition metal oxides, we apply the PBE+*U* method, where *U* values are determined from Ref. 34. The energy cutoff of the plane-wave basis and k-points of each material are selected by conducting convergence test to satisfy the energy (10 meV/atom) and pressure (10 kbar) criteria. For the hybrid calculation, we use HSE06 scheme with fixed mixing parameter of 0.25.^[36]

3.2.2 Band gap

The density functional theory has a disadvantage that it evaluates the band gap much smaller than the experiment.^[47] To overcome the band gap underestimation, hybrid calculation or GW approximation should be used, which can estimate the more accurate band gap but require much more computational cost than conventional GGA method. However, these schemes are not suitable to perform the high-throughput calculation due to their too much computation time. Thus, we use HSE@GGA method in which structure relaxation is conducted in GGA method and band gap is estimated by one-shot hybrid calculation.^[48] By using the method, we can obtain accurate band gap of massive materials.

As we mentioned, GGA scheme underestimates band gap of materials. However, the band structure with GGA is similar to the that with hybrid calculation or GW approximation. Therefore, we first calculate the band structure using the GGA functional and then find the maximum point of valence band and minimum point of the conduction band. Finally, we evaluate band gap by calculating the energy level of only these two points using hybrid calculation. The lattice parameters with GGA calculation are generally longer than that with hybrid calculation. However, the difference is not significant and it does not lead to a big difference of band gap. Also, computational cost to perform the structure optimization using hybrid scheme is quite expensive. Thus, we use structure calculated by GGA scheme and only electronic structure is optimized. Figure 3.1 shows the experimental and theoretical band gaps of the oxides. The results of

HSE@GGA method, marked with a red circle, are in good agreements with the band gap with full hybrid calculation. Also, HSE@GGA scheme gives more reliable band gap rather than GGA and LDA approach. This results show that HSE@GGA method is accurate and efficient to predict band gap.

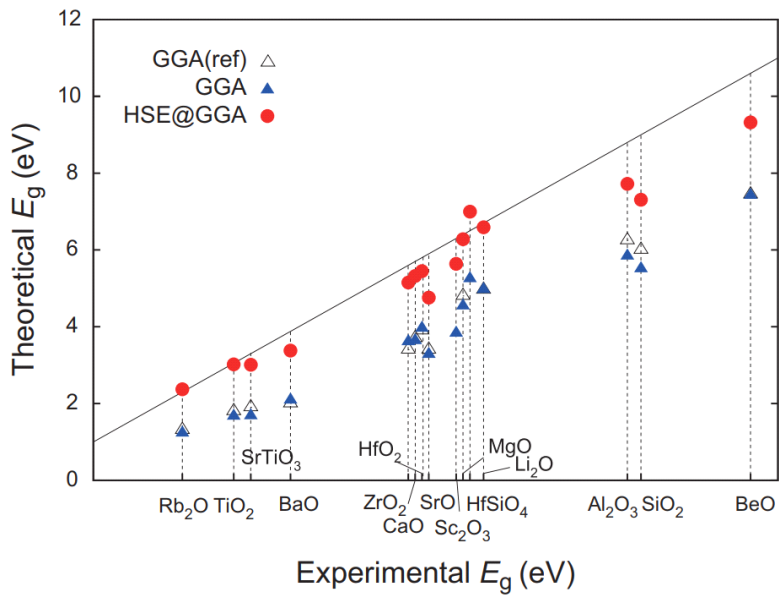


Figure 3.1 Calculated band gap Vs. experimental band gap. The solid line means perfect agreements with the experiment gap. HSE@GGA is the band gap calculated by hybrid scheme with lattice parameter from GGA scheme.^[48]

3.2.3 Effective mass

Effective mass is a physical quantity used to describe the movement of electrons in a solid as if the free electrons move according to the classical physics. The electrons in a solid move differently than free electrons since the electrons inside the solid are influenced by surrounding electrons and it is impossible to predict the movement of electrons considering all ionic and electronic interaction. Therefore, approximation should be used. In the method using effective mass, the effect of the interactions are approximated as if the mass of the electrons changes heavily or lightly. The effective mass tensor is defined as

$$m^*_{ij} = \hbar^2 \left[\frac{\delta^2 E}{\delta k_i \delta k_j} \right]^{-1}, \quad (3.1)$$

where, k_j is wavevector along to i direction and E is energy. In the most of oxides, the E - \mathbf{k} relation at the conduction band minimum is quadratic and isotropic as shown in Figure 3.2 since the conduction band mainly consists of metal s orbital. Thus, the electron effective mass is also isotropic and consistent in vicinity of conduction band minimum. In addition, it can be easily estimated using one-dimensional model. At the valence band maximum, however, the E - \mathbf{k} relation is much more complex rather than the relation at the conduction band minimum. Fig 3.2 shows that the E - \mathbf{k} relation at the valence band top is anisotropic and valence band top consists of two or more bands. In this case, we should consider not only first band but also the other bands to estimate the reliable effective mass.

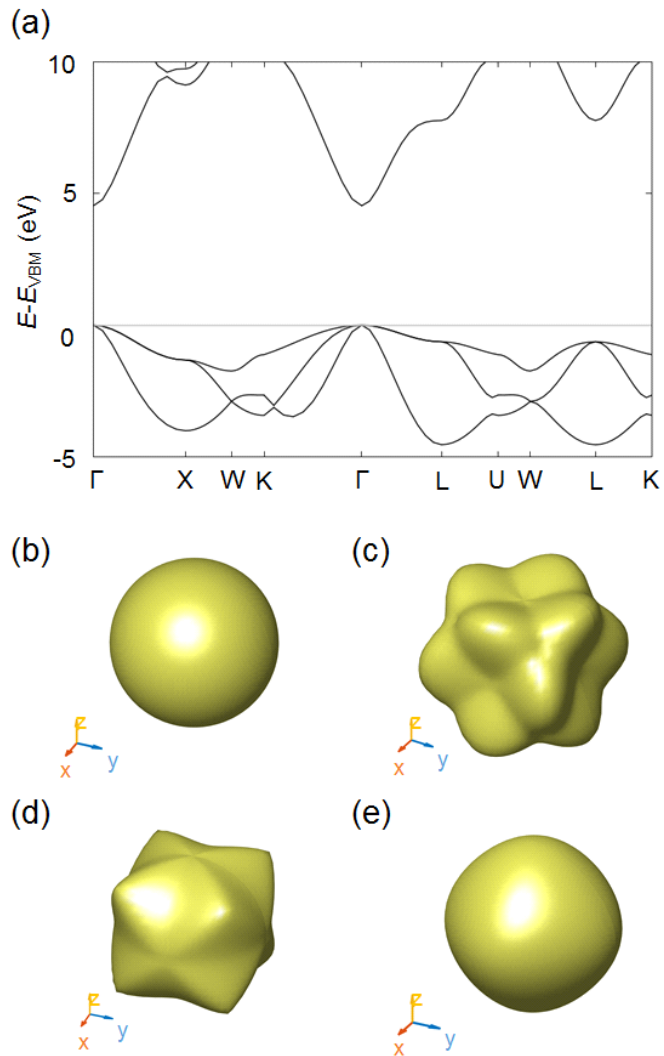


Figure 3.2 (a) Band structure of MgO. Constant energy surface for (b) conduction band at the conduction band minimum and (c-e) three valence bands at the valence band maximum.

In this study, we calculate the effective mass considering the Fermi distribution of electrons or holes using following equation.

$$\langle m^*_{ij} \rangle = \hbar^2 \left[\frac{\sum_n \int d\mathbf{k} \frac{\delta^2 E_{n\mathbf{k}}}{\delta k_i \delta k_j} f_{n\mathbf{k}}}{\sum_n \int d\mathbf{k} f_{n\mathbf{k}}} \right]^{-1}, \quad (3.2)$$

where, f is Fermi distribution and n is band index. To solve the equation, we should consider the entire region in the reciprocal space and all band. Additionally, the distance between sampling points is reduced to enhance the accuracy. However, it is difficult to calculate the band energy at the numerous k-points for high-throughput calculation. Thus, we propose the efficient scheme which does not sacrifice computation accuracy while improving computational efficiency. According to the Fermi distribution, the number of electrons (or holes) increases or decreases dramatically with increasing the difference between the energy of electrons (or holes) and Fermi energy (E_F). It means that we can calculate the accurate effective mass using the limited number of k-points at which the electron (or hole) distribution is higher than 0.01. Figure 3.3 shows the energy region (blue shadow) where the Fermi distribution is lower than 0.99 at 300K and $E_F = E_{VBM}$ and the k-points region (red shadow) corresponding to the energy region. The k-points region we used is quite narrow so we can reduce the computational cost dramatically.

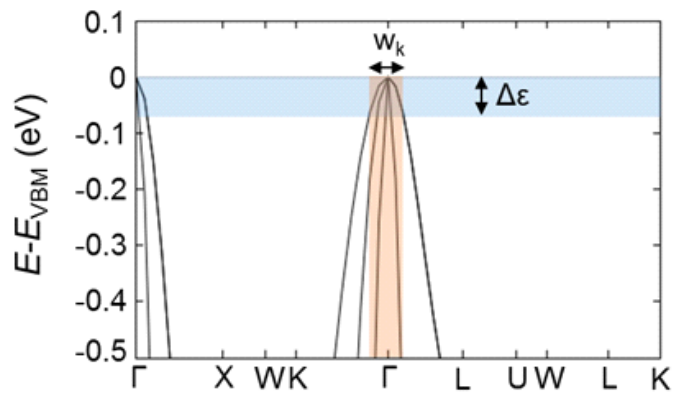


Figure 3.3 Band structure of MgO in vicinity of E_{VBM} . Blue shadow indicate the energy region where f is lower than 0.99 at 300 K and $E_F = E_{VBM}$. Red shadow indicate the k-points region corresponding to the energy region.

In this study, we estimate the effective mass using GGA method. As we mentioned in band gap section, GGA scheme has a critical problem, band gap underestimation and HSE scheme is needed. In spite of the underestimation of band gap in GGA scheme, the accuracy of effective mass is not inferior to that using HSE scheme. This is because the shape of bands are almost identical even though the band structures are estimated using different methods as illustrated in Figure 3.4.

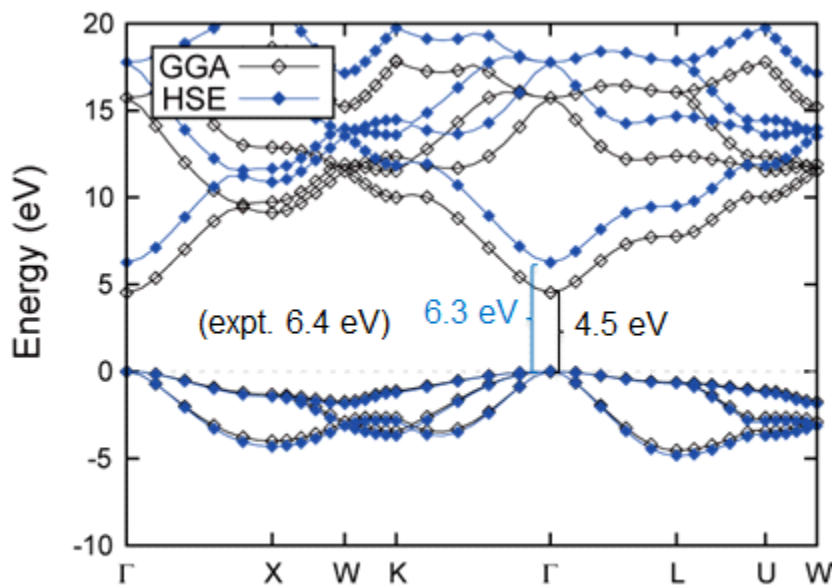


Figure 3.4 Band structure of MgO calculated by GGA and HSE scheme. The valence band top is set to zero.

3.2.4 Branch-point energy

In the semiconductor-semiconductor interface, energy bands and wave functions are different to their bulk states values. These interface states can be derived from virtual gap states (ViGS) and their dominant character becomes acceptor-like states near the valence band or donor-like states close to the conduction band. The certain energy state where the dominant character of ViGS changes is defined as branch point energy (BPE).^[49] BPE can be estimated by the following equation.

$$E_{\text{BP}} = \frac{1}{2N_{\mathbf{k}}} \sum_{\mathbf{k}} \left[\frac{1}{N_{\text{CB}}} \sum_i^{N_{\text{CB}}} \varepsilon_{c,i}(\mathbf{k}) + \frac{1}{N_{\text{VB}}} \sum_j^{N_{\text{VB}}} \varepsilon_{v,j}(\mathbf{k}) \right], \quad (3.3)$$

where N_{CB} (N_{VB}) indicates the number of conduction (valence) bands for calculation and $\varepsilon_{c,i}$ ($\varepsilon_{v,j}$) is energy state of i th conduction band (j th valence band) at \mathbf{k} . Figure 3.5 shows the band structure of MgO and its branch point energy. BPE can be used to describe the band alignment of ideal semiconductor interface. However, there is no certainty that it can be used to align the energy level with respect to vacuum level.

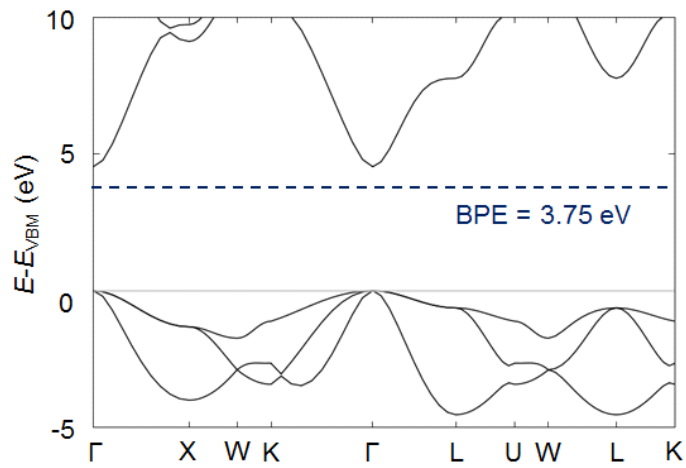


Figure 3.5 Band structure of MgO. Blue dashed line indicates the branch point energy (E_{VBM} is set to zero).

3.3 Hydrogen descriptor

3.3.1 Limitation of previous descriptor

In the previous studies, band gap, hole effective mass and branch point energy are used as descriptors to discover new p-type transparent oxide semiconductors by high-throughput screening. However, the proposed materials in these studies cannot be validated experimentally, which implies that they used inappropriate or insufficient descriptors. Thus, we perform the verification of the descriptors. Figure 3.6 shows the hole effective masses and branch point energies of well-known n-type and p-type oxides. The result indicates that previous descriptors fail to distinguish between p-type and n-type semiconducting oxides. For example, ZnRh_2O_4 has higher hole effective mass than most of n-type oxides in spite of its p-type character. Also, TiO_2 has low branch point energy rather than most of p-type oxides but only n-type conductivity is observed in experiment. $\text{Ba}_2\text{BiTaO}_6$ and SnNb_2O_6 (black square in Figure 3.6) also show the limitation of previous descriptors.^[23,50] According to the previous descriptors, these materials can be good p-type TSOs superior to the known p-type oxides. However, they showed insulating characteristics experimentally, and $\text{Ba}_2\text{BiTaO}_6$ has very low electrical conductivity through external doping. These results show that it is difficult to find new p-type semiconductors using previous descriptors.

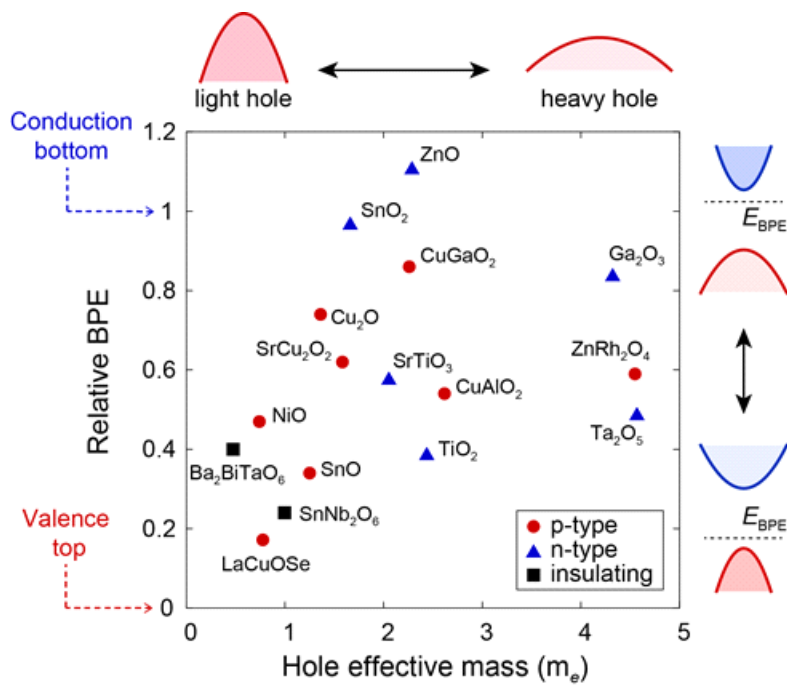


Figure 3.6 Comparison of hole effective mass and relative BPE ($= [BPE - E_{VBM}]/E_g$) of known p-type and n-type oxides.

However, this result does not imply that it is impossible to find a new p-type semiconductor through first principles calculations. The defect formation energies of these two materials in Figure 3.7 show that both materials would have insulating properties. In the figure, the chemical potential of each element is defined as the condition for having the p-type characteristic, that is the value in the oxygen-rich environment. In the case of $\text{Ba}_2\text{BiTaO}_6$, Bi vacancy and Ba vacancy are intrinsic defects that can generate holes because they can easily receive electrons. However, Bi_{Ta} substitutional defect which plays a role as donor are more stable near the valence band, so holes formed by Bi vacancies or Ba vacancies are easily compensated. Therefore, $\text{Ba}_2\text{BiTaO}_6$ has an insulator-like property. SnNb_2O_6 can also form holes by Sn vacancy or Sn_{Nb} defect, but easily compensate holes by O vacancies or Nb_{Sn} defect. As a result, the conduction characteristics of the material can be understood successfully through the defect formation energies. In addition, we should find new descriptors having comparable accuracy with defect formation energy to discover reliable p-type candidates using high-throughput screening.

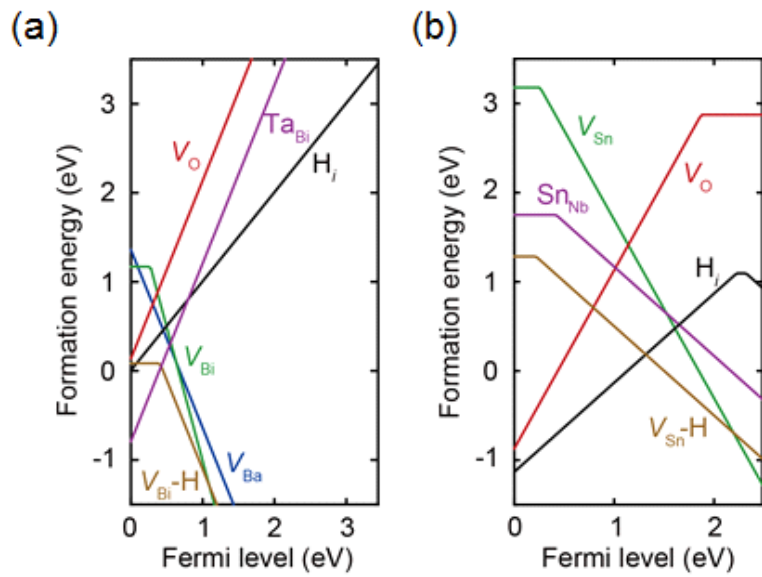


Figure 3.7 Defect formation energies of (a) $\text{Ba}_2\text{BiTaO}_6$ and (b) SnNb_2O_6 .

3.3.2 Defect formation energies of known semiconducting oxides

In order to find a new descriptor, we estimate the defect formation energies of well-known p-type and n-type oxide semiconductors. Figure 3.8 are defect formation energy diagrams of SnO, Cu₂O, and CuAlO₂ which are well known p-type oxide semiconductors. These figures show that the acceptor-like defects are more stable over all region rather than donor like defects. $V_{\text{Sn-H}}$ in SnO, V_{Cu} in Cu₂O and V_{Cu} and Cu_{Al} in CuAlO₂ are the acceptor-like defects that can generate holes. In the defect formation energy diagrams, not only intrinsic defects but also hydrogen related defects are illustrated because it is difficult to control the hydrogen in a real experimental environment. From the defect formation energy, we know another common rule that hydrogen-interstitial (H_i) defects have a role to compensate the holes by donating electrons. In all three materials, the formation energy of H_i defect or hydrogen-substitutional defects in the oxygen sites (H_O) are lowest among the donor-like defects. This shows that the hydrogen interstitial defect plays an important role in determining the p-type oxide semiconductor.

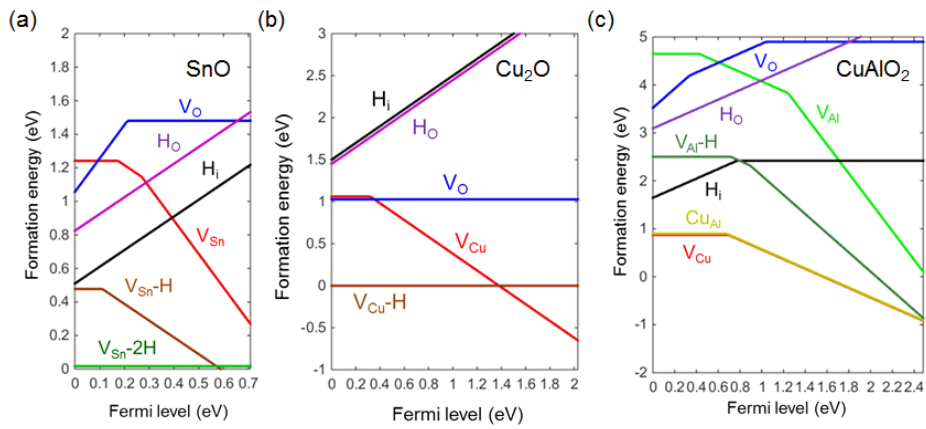


Figure 3.8 Defect formation energies of known p-type materials. (a) SnO, (b) Cu_2O and (c) $CuAlO_2$.

The importance of hydrogen related defect is also displayed in Figure 3.9 which show the defect formation energy of well known n-type oxides. We use the chemical potentials in metal-rich (oxygen-poor) condition in which intrinsic n-type defects are easily formed. In the result, oxygen vacancy is most stable defect among the intrinsic defect in these oxides, which imply that electrons can be generate. Hydrogen-related defect also show that donor like defects are more stable than acceptor like defects. Another important thing is that hydrogen-related defect is most stable defect among the donor like defect same to the p-type oxides in Figure 3.8. As a result, the n-type and p-type can be classified using the hydrogen related defect, especially H_i defect.

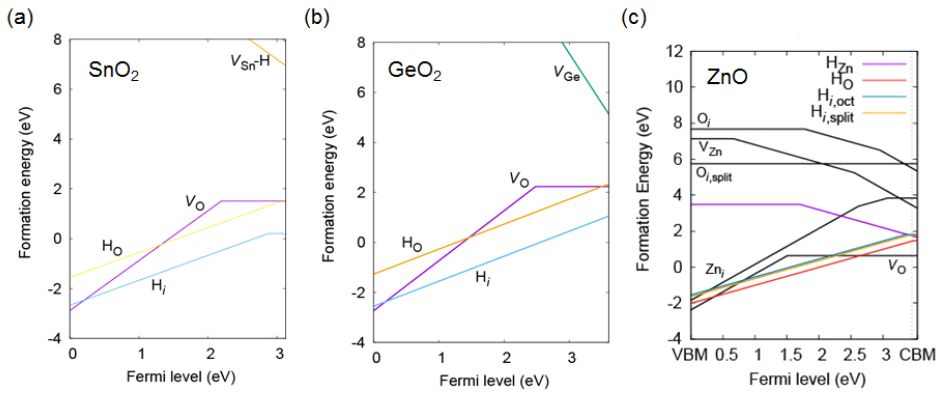


Figure 3.9 Defect formation energies of known n-type materials. (a) SnO₂, (b) GeO₂ and (c) ZnO.

3.3.3 Hydrogen descriptor for p-type oxide screening

We propose a new hydrogen descriptor for p-type oxides which is defined as the defect formation energy of hydrogen interstitial in +1 charge state (H_i^+) with the Fermi level at the valence top (FEH hereafter). For convenience, the chemical potential of hydrogen is set from the H_2 molecular energy. Figure 3.10 shows the definition of FEH in the formation-energy diagram. There are two reasons that FEH can be reliable descriptor for p-type oxides. One is that hydrogen interstitial defect can be dominant defect to compensate holes in experiment.^[51,52] Second, the FEH correlates with the valence band level with respect to vacuum level since hydrogen transfers an electron to the VBM according to the definition of FEH. The H_i^+ is always located near the oxygen atom forming O-H bond as illustrated in Figure 3.10 since oxygen is negatively charged.

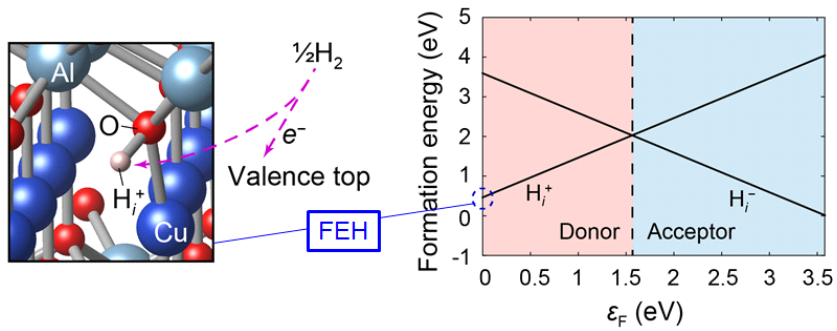


Figure 3.10 The left figure shows the atomistic configuration of H_i^+ in $CuAlO_2$. The right figure shows defect formation energy of H_i in $CuAlO_2$ as a function of Fermi level (ϵ_F). The vertical dashed line indicates the hydrogen transition level.^[26]

In order to verify the reliability, we estimate the FEH of the same oxides as in Figure 3.6. In Figure 3.11, we show that FEH can clearly distinguish the p-type and n-type oxides with the decision boundary at $\text{FEH} = -1 \text{ eV}$. Additionally, the insulating materials such as $\text{Ba}_2\text{BiTaO}_6$ and SnNb_2O_6 are placed in the middle range of FEH. This result shows that FEH has sufficient performance to be used for high-throughput screening for p-type. Furthermore, we can explain the high conductivity of SnO and Cu_2O using FEH. Also, the p-type conductivity of ZnO by nitrogen doping^[53,54] can be shown by highest FEH of ZnO among n-type oxides. We note that high FEH is directly connected to the performance of p-type but lower FEH does not mean that it become a good n-type oxide. Figure 3.12 show that FEH is strongly correlated to the experimental ionization potential (IP). Since the formation energy of a hole is determined by the energy level of VBM, FEH can be a good descriptor for p-type oxides. Additionally, in the hydrogen poor condition (p-type condition), FEH is always higher than 0 eV. It implies that the generation of H_i^+ is suppressed and holes are not compensated.

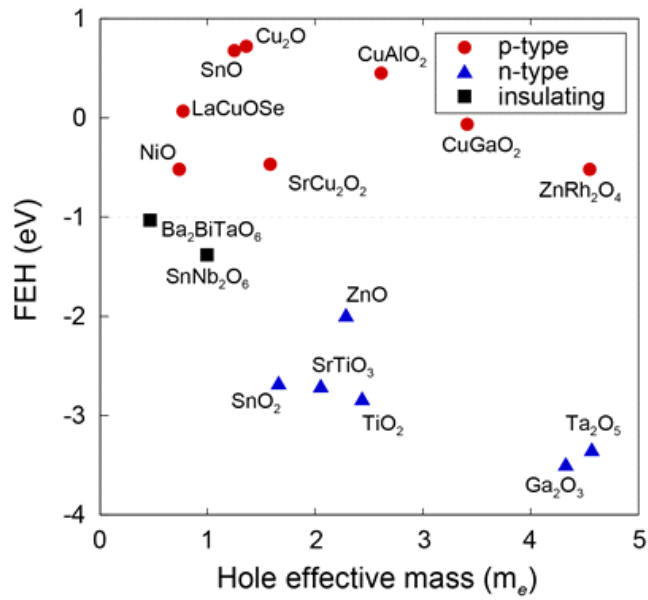


Figure 3.11 FEH versus hole effective mass of oxides presented in Figure 3.6.^[26]

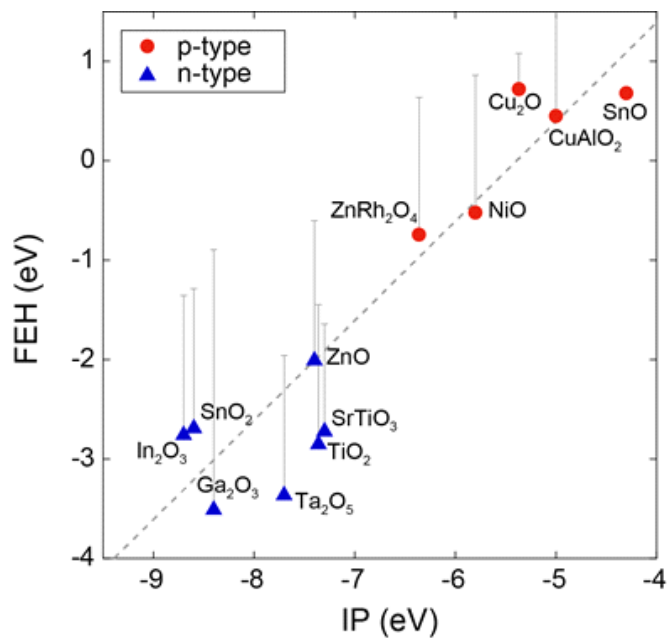


Figure 3.12 Comparison of FEH versus ionization potential in experiment.^[55-58] The grey error-bars indicates the region of hydrogen interstitial defect formation energy depending on the chemical potential.^[26]

The position of VBM with respect to the vacuum level can be a indicator for p-type oxides. In this aspect, $H(+/-)$ level^[59] can be also used to distinguish p-type and n-type oxides. In Figure 3.13, we compare FEH and $H(+/-)$ level for several oxides of which doping type is known. Two quantities has a linear correlation to some extent, but FEH classifies conduction type of oxides more clearly. Also FEH is computationally more efficient than $H(+/-)$.

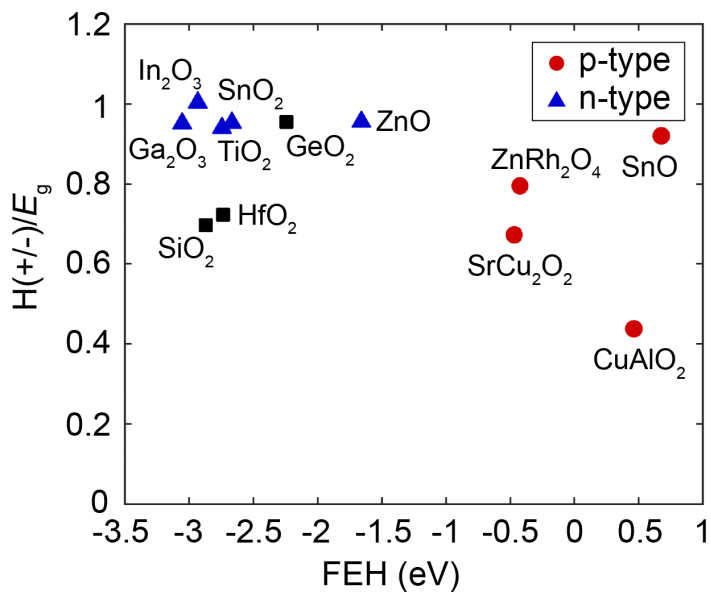


Figure 3.13 FEH versus $H(+/-)$ level.^[26]

3.3.4 Automatic procedure for hydrogen descriptor

For high-throughput screening calculation, the computational procedure should be automated. Thus, we develop a code to calculate the FEH automatically. In this process, we couple the conventional PBE scheme and hybrid (HSE) scheme to improve the efficiency of calculation with high accuracy. The conventional PBE method can describe the structural and electrical properties efficiently. However, the underestimation of band gap can lead to serious problem to calculate the charged defect formation energy. Thus, we need to use a HSE method to overcome the problem. However, HSE calculations are not suitable for high-throughput calculation because they require too much computation time. In particular, defect calculation is performed using the supercell including many atoms by repeating the basic lattice instead of the basic lattice. This also greatly increases the computational cost, so it is almost impossible to obtain a large number of supercell computation results using the HSE method. In order to overcome this problem, PBE and HSE methods are used in parallel for the unit cell calculation, and only PBE scheme is used for the supercell calculation.

Figure 3.14 is a simplified flowchart of the automation process. The first step is to get information about the structure from the ICSD website.^[60] In the next step, optimized structures are obtained using PBE and HSE methods respectively. Since it is costly to calculate the band structure by the HSE method, the band structure is calculated by the PBE method and we find the k-point having the minimum conduction band energy and the k-point having the maximum valence

band energy. Then we estimate the energy state at the k-points using HSE scheme. In this way, it is possible to calculate the band gap accurately and quickly. The hole effective mass is calculated by the PBE method.

As mentioned above, the supercell calculation also proceeds using the PBE method. To estimate the reliable defect formation energy of interstitial defects, we should perform the multiple calculations since interstitial defect can be located at various sites and each structure should be optimized to compare the formation energy and to find the most stable location. However, it is too expensive to perform the all simulation processes using first principle calculations. Therefore, the initial position of hydrogen interstitial defect is predicted through the Coulomb potential information, and the stabilization process is performed for only one position. The validity of this method is proved that this position is always the most stable site even if we calculated the energy at several locations.

To overcome the underestimation of band gap in PBE, we estimate the FEH considering the VBM shift between PBE and HSE scheme. The corrected FEH is calculated by following equation as

$$\text{FEH}_{\text{corr}} = \text{FEH}_{\text{PBE}} + \Delta\text{VBM} - 0.27 \text{ eV}, \quad (3.4)$$

where FEH_{PBE} indicate the FEH calculated by PBE scheme and ΔVBM is the gap in ε_{VBM} between PBE(+ U) and HSE calculation with respect to the common reference point^[61]. The energy level at VBM is estimated by the unit-cell calculation. The additional term (-0.27 eV) can be explained by over binding energy of O-H bond in PBE

functional. In Figure 3.15, the corrected FEH from PBE functional is in good agreement with the FHE_{HSE} , which shows the reliability of this correction scheme. After this, the FEH is calculated by equation 3.4.

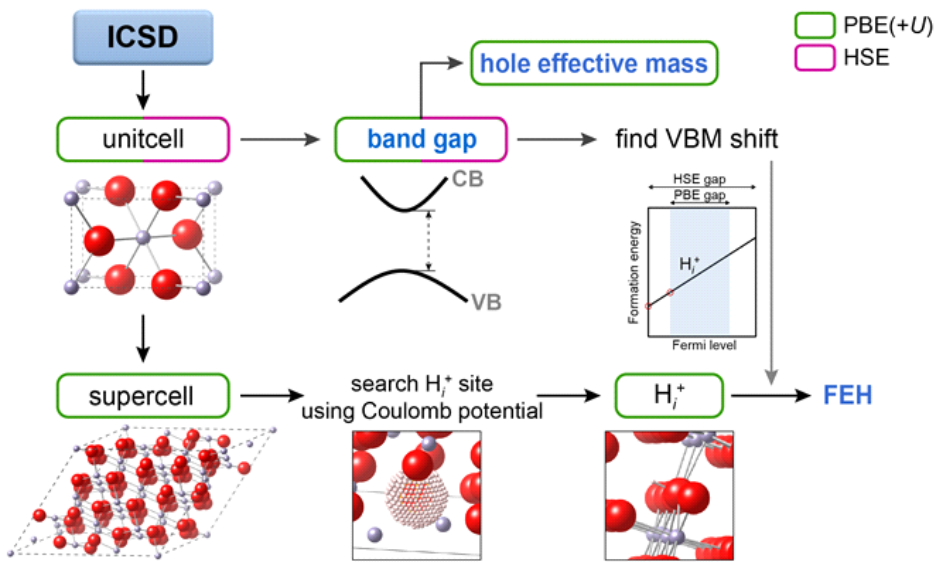


Figure 3.14 Schematic work flow to estimate FEH.^[26]

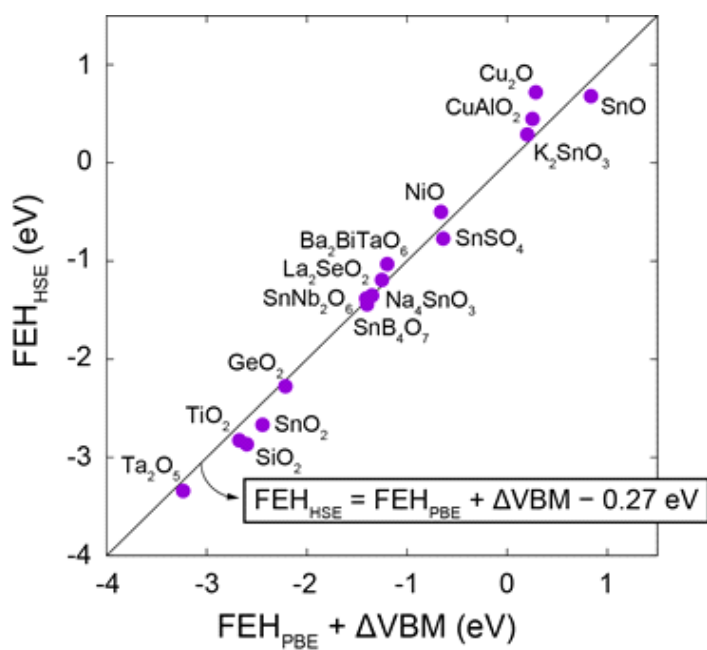


Figure 3.15 Comparison of FEH estimated by PBE scheme with VBM correction and full HSE method.^[26]

3.4 High-throughput screening of p-type oxides

3.4.1 Screening over binary oxides

We performed high-throughput screening calculations to find new p-type oxide semiconductors using the hydrogen descriptor. In the first step, the calculations for most binary materials were performed using automated procedures. When polymorphism of a specific composition ratio exists, the most stable structure is calculated preferentially, and an automatic calculation is also performed for polymorphs with energy lower than 10 meV/atom. Figure 3.16 shows FEH and hole effective mass for binary materials. The optical band gap of each material is expressed by the transmittance of each point. The completely transparent point is a material with an optical band gap greater than 3.1 eV, and the completely opaque material means an optical band gap smaller than 1.8 eV. Well-known p-type oxide semiconductors are marked in orange, and all of these materials have a FEH greater than -1 eV. However, with the exception of well-known substances, no substances with FEH values greater than -1 eV is found. This result shows that it is very difficult to find a new binary p-type oxide semiconductor.

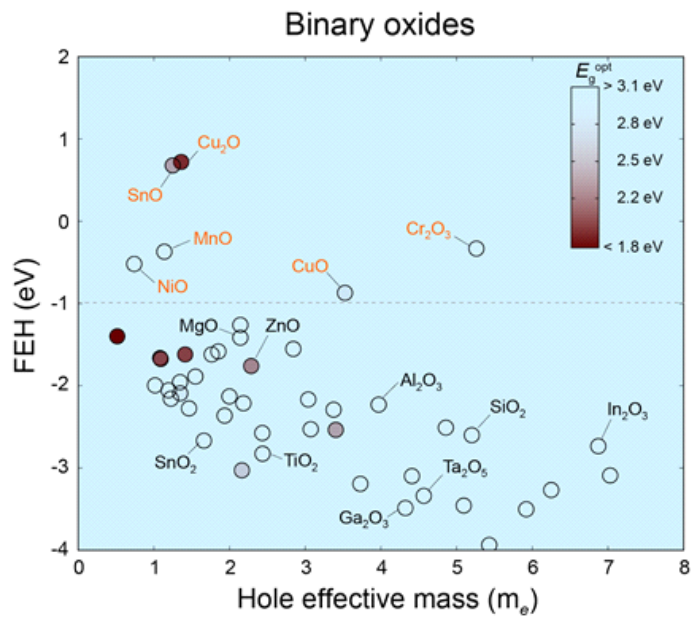


Figure 3.16 FEH and hole effective mass for binary oxides. Known p-type oxides are indicated in orange. The transparency of each material shows its optical band gap.^[26]

3.4.2 Screening over ternary oxides

To search for new p-type oxide semiconductors, the material search space was extended to the ternary material group. Although combining the PBE and HSE methods improves the calculation speed, calculating the defect energies still requires much computational cost. Therefore it is very difficult to carry out FEH calculation for all ternary substances. So we limited the material search space based on the properties of known p-type oxide semiconductors. The first condition is that the valence band is a mixture of contributions by oxygen atoms and metal atoms. The hybridized band states are delocalized and raise the position of VBM. For example, in SnO, the valence band consists of Sn $4s^2$ orbital and oxygen $2p$ orbitals.^[62] Also, Cu^{1+} with $3d^{10}$ configuration forms the valence states in Cu_2O and CuAlO_2 .^[63] LaCuOSe with the highest hole conductivity^[17] gives another design principles for p-type that another anions character at VBM enhances the p-type properties. In the case of LaCuOSe , Se^{2-} states at VBM raises the VBM energy and reduces hole effective mass due to larger orbital size than O^{2-} .^[64] Therefore, oxychalcogenides with multi-anion character should be considered as p-type candidates. However, polyanion compounds such as $\text{Sn}(\text{SO}_4)$ has lower FEH than their oxide counterparts.

From the p-type principles of known p-type oxides, we restrict the screening space of ternary compounds to Sn^{2+} - and Cu^{1+} -bearing ternary oxides and ternary oxychalcogenides. In addition, we consider only stable phases which are chosen by the material database.^[48] As a result, we estimate the FEH for 40 materials as shown in Figure

3.17. As with the binary results, known ternary p-type oxides (indicated in orange) including delafossite structures satisfy the p-type condition ($FEH > -1$ eV), which shows again the validity of FEH. Figure 3.17 displays several p-type candidates which have not been tested in experiment as far as we are aware. The detailed data for p-type candidates are presented in Table 1.

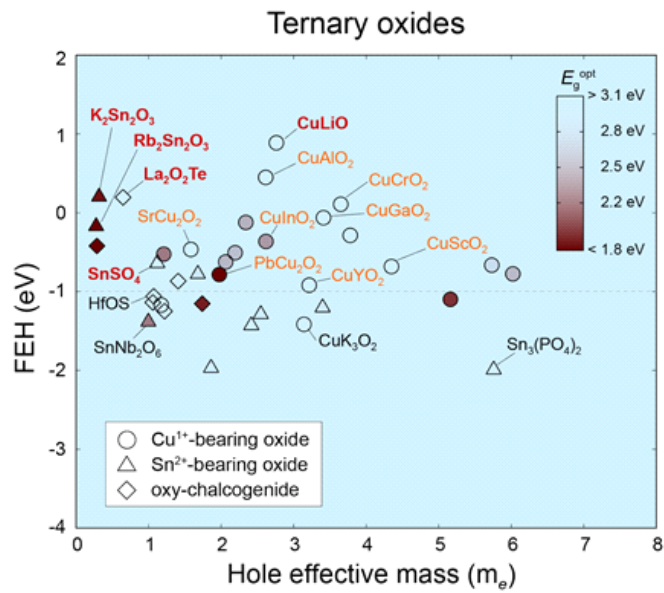


Figure 3.17 FEH and hole effective mass for ternary oxides. Promising p-type candidates and known p-type oxides are marked in red-bold and orange, respectively. The transparency of each material shows its optical band gap.^[26]

Table 1. p-type candidates satisfying $\text{FEH} > -1$ eV. (m_1 , m_2 , m_3) indicate effective masses along the principal axis and m_{avg} is their harmonic average.^[26]

Type	Name	FEH (eV)	Hole effective mass (m_e)		Optical band gap (eV)
			m_{avg}	(m_1 , m_2 , m_3)	
Sn ²⁺ -bearing oxides	K ₂ Sn ₂ O ₃	0.20	0.32	(0.32, 0.32, 0.32)	1.89
	Rb ₂ Sn ₂ O ₃	-0.17	0.28	(0.36, 0.25, 0.25)	1.66
	SnSO ₄	-0.64	1.12	(0.67, 7.51, 0.94)	5.40
	Sn ₄ O ₂ F ₄	-0.78	1.68	(2.23, 1.18, 2.04)	3.05
Cu ¹⁺ -bearing oxides	CuLiO	0.89	2.76	(2.59, 2.59, 3.22)	3.10
	CuNaO	0.08	9.01	(18.42, 18.41, 4.46)	2.96
	BaCu ₂ O ₂	-0.12	2.34	(4.96, 4.96, 1.14)	2.75
	Cu ₂ SO ₄	-0.29	3.78	(2.33, 4.43, 7.23)	3.19
	Cu ₂ NaO ₂	-0.51	2.19	(9.11, 156.7, 0.80)	2.83
	CsCuO	-0.53	1.21	(7.68, 0.46, 5.54)	2.45
	Cu ₃ PO ₄	-0.56	3.50	(2.16, 17.67, 2.96)	2.55
	Cu ₂ LiO ₂	-0.62	2.06	(43.49, 1.40, 1.40)	2.79
	CuKO	-0.66	5.73	(18.93, 18.93, 2.39)	2.99
	CuRbO	-0.78	6.02	(2.03, 329.4, 329.3)	2.80
	Cu ₃ VO ₄	-0.79	2.55	(2.70, 2.52, 2.45)	2.01
Oxychalcogenides	La ₂ O ₂ Te	0.20	0.65	(1.05, 0.31, 2.25)	3.12
	La ₄ O ₄ Se ₃	-0.42	0.29	(0.10, 488.0, 47.15)	1.68
	Y ₂ OS ₂	-0.87	1.41	(2.56, 0.82, 1.90)	3.67

3.4.3 Defect formation energy for candidates

In the promising p-type candidates, there are several non-delafossite Cu^{1+} -bearing ternary oxides such as $\text{CuM}'\text{O}$ ($M' = \text{Li, Na, K, Rb, Cs}$). All the materials except for CuCsO ($Cmcm$) have the same symmetry ($I4m2$) where Cu^{1+} forms Cu_4O_4 four-membered rings as illustrated in Figure 3.18a. Among $\text{CuM}'\text{O}$ compounds, CuLiO is the most promising candidate due to its highest FEH (0.89 eV) in the screened ternary oxides and other $\text{CuM}'\text{O}$ compounds have lower FEH with increase of atomic number of M' . Therefore, it is expected that CuLiO has higher hole concentration than CuAlO_2 . Also, the averaged m_h ($2.76 m_e$) is comparable with the CuAlO_2 ($2.66 m_e$). The formation enthalpy (-0.23 eV) from binary phases, $\frac{1}{2}\text{Li}_2\text{O}$ and $\frac{1}{2}\text{Cu}_2\text{O}$, shows its thermodynamic stability. The defect formation energies in Figure 3.18c present that Li vacancy (V_{Li}) is a major source of holes in CuLiO since its formation energy is lower than V_{Cu} . It is different to the delafossite materials of which dominant acceptor is V_{Cu} . Additionally, the calculated (0/−) transition level of V_{Li} (0.24 eV) is lower than Cu vacancy in known oxides ($0.4 \sim 0.7$ eV)^[65,66], which imply that CuLiO can be a good p-type oxide.

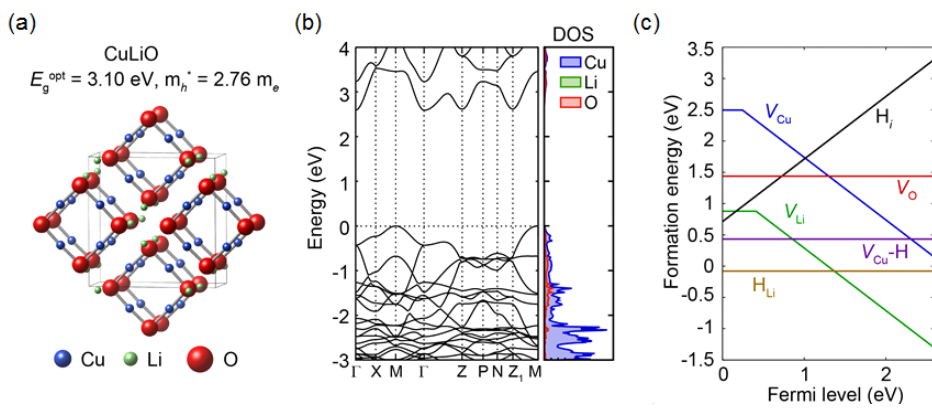


Figure 3.18 (a) The atomic structure of CuLiO. (b) Band diagram and partial density of states using gap correction with HSE scheme. (c) The defect formation energy diagram at the oxygen-rich condition.^[26]

Next, we perform high-throughput screening for Sn^{2+} -bearing oxides of which valence band consists of $\text{Sn-}4s^2$. Figure 3.17 presents several p-type candidates satisfying FEH condition. However, there is no material where FEH is higher than SnO. It might be because the stronger interaction between the other cation and oxygen can result in wider band gap and lower valence band level. Therefore, in Sn^{2+} -bearing oxides, it might be difficult to be transparent and have high hole dopability, simultaneously. In the aspect of FEH, noticeable candidates are $\text{K}_2\text{Sn}_2\text{O}_3$ and $\text{Rb}_2\text{Sn}_2\text{O}_3$ which were already reported in the previous study^[22]. However, they are expected as opaque material due to their low optical band gap. SnSO_4 is another p-type candidate which has high optical band gap (5.12 eV) and low hole effective mass ($1.12 m_e$). Figure 3.19a presents the crystal structure of SnSO_4 . Due to the polyanion group, $(\text{SO}_4)^{2-}$, its band gap is much higher than SnO. However, the polyanion group also drops the VBM level, which result in the lower FEH (-0.8 eV) than SnO. Therefore, we expect that it has lower hole concentration than SnO. The defect calculation supports its low hole concentration since the H_i^+ defect partially compensates the acceptors as $V_{\text{Sn}}\text{-H}$. As a result, polyanion group such as $(\text{SO}_4)^{2-}$ and $(\text{PO}_4)^{3-}$ is not a good choice in the aspect of hole concentration.

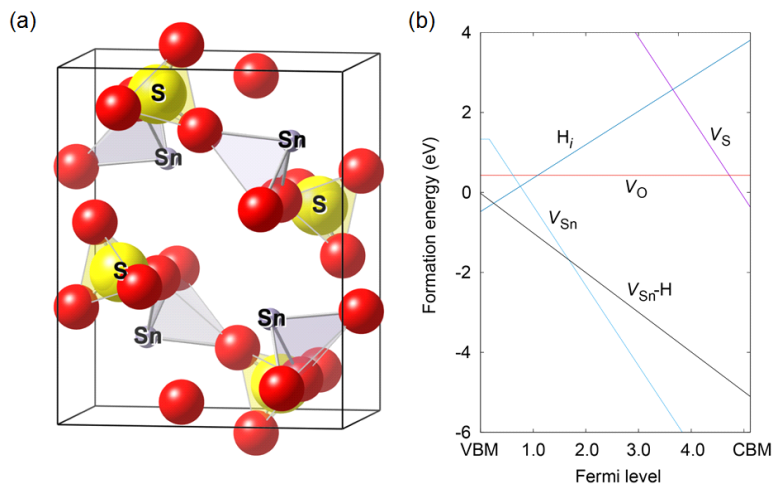


Figure 3.19 (a) The atomic structure of SnSO_4 . (b) The defect formation energy diagram at the oxygen-rich condition.^[26]

Oxychalcogenides are the last searching space for p-type. In the ICSD, however, most of compounds including both O and chalcogen elements (S, Se and Te) are polyanion compounds rather than multi-anion compounds that chalcogen elements are negatively charged. In spite of the small number of oxychalcogenides, the most promising candidate, $\text{La}_2\text{O}_2\text{Te}$, is searched in this group. $\text{La}_2\text{O}_2\text{Te}$ has high FEH (0.2 eV), high optical band gap ($E_g^{\text{opt}} > 3$ eV) and low hole effective mass ($0.65 m_e$). In addition, its stability is confirmed by the formation enthalpy (-0.83 eV) from binary oxides, $\frac{1}{2}\text{La}_2\text{O}_3$ and $\frac{1}{2}\text{La}_2\text{Te}_3$. $\text{La}_2\text{O}_2\text{Te}$ is formed by alternating O and Te layers as shown in Figure 3.20a. In addition, VBM mainly consists of Te-5p character in Figure 3.20b, which results in the anisotropic hole effective mass. The defect calculation in Figure 3.20c show that $\text{La}_2\text{O}_2\text{Te}$ could be generate holes at the oxygen-rich condition. $V_{\text{La}-2\text{H}}$ is the major acceptor among intrinsic defects of which (0/-) transition level (0.13 eV) is close to the VBM. However, $V_{\text{La}-2\text{H}}$ is partially compensated by hydrogen defect. Thus, we attempt to find possible external dopant and discover a reliable external dopant, Ca_{La} . In Figure 3.20c, $\text{Ca}_{\text{La}}^{1-}$ is more stable than the others and it behaves a shallow acceptor whose (0/-) transition level is similar to $V_{\text{La}-2\text{H}}$. In the previous study,^[24] La_2SeO_2 whose structure is same to $\text{La}_2\text{O}_2\text{Te}$ is suggested as a promising p-type candidate. However, it does not satisfy the FEH condition (-1.25 eV).

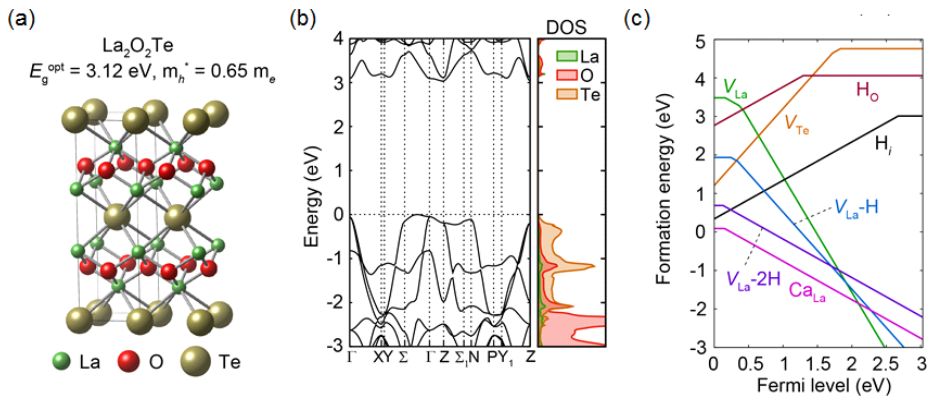


Figure 3.20 (a) The atomic structure of $\text{La}_2\text{O}_2\text{Te}$. (b) Band diagram and partial density of states using gap correction with HSE scheme. (c) The defect formation energy diagram at the oxygen-rich condition.^[26]

3.5 Summary

A new hydrogen related descriptor has been proposed to find new p-type oxide semiconductors. We have verified that the descriptor has high reliability by calculating the well known p-type and n-type oxide semiconductors, and confirmed that all known p-type oxide semiconductors are distinguished as hydrogen descriptor. Next, we developed an automated code that can calculate the hydrogen selector and performed high-throughput screening calculations on the binary materials. However, a p-type oxide semiconductor candidate was not found in binary materials. In addition, screening calculations were performed on the ternary substance group based on the characteristics of the conventional p-type semiconductor oxide. We proposed a novel p-type semiconductor candidate such as CuLiO or $\text{La}_2\text{O}_2\text{Te}$. The analysis of the electronic structure revealed the reason why these materials can be p-type semiconducting oxide, and it is confirmed that defects which can generate holes are present through defect energy analysis. This material is likely to be a p-type oxide semiconductor and will need to be verified through further experiments.

High-throughput screening of p-type oxides using material database

4.1 Introduction

The high-throughput screening method based on the density functional theory has been used to accelerate the discovery of functional materials.^[22-26,48,67-70] Especially, recent development of materials database^[71-73] enable rapid screening with DFT simulation.^[22,24,68-70] In the previous chapter, we propose a reliable descriptor, FEH, which can clearly distinguish the known p-type and n-type oxides. Also, we reduce the computational cost by combining PBE and HSE computational scheme. Nevertheless, it still requires high computational cost comparing to bulk properties such as band gap and effective mass. To realize the unlimited screening space, we need to find cost effective descriptor.

In this chapter, we propose an extremely fast approach to identify the p-type candidates from the over 17,625 oxides reported in the AFLOW database.^[71] For quick and coarse screening, we search descriptors from elemental information and quantum mechanical data in the materials database, which are band gap and oxygen partial weight at the valence band top for p-type transparent oxides. We reduce computational cost by evaluating the FEH for only survived

candidates. Through the multi-step high-throughput screening, we identify 47 p-type candidates such as Na_2PtO_2 , $\text{La}_2\text{O}_2\text{S}_2$, Sr_3BPO_3 , Ba_3BPO_3 and $\text{La}_2\text{SiO}_4\text{Se}$. Additionally, we estimate the defect formation energies to examine the source of holes.

4.2 Computational methods

4.2.1 Density functional theory

We perform the density functional theory calculation using Vienna Ab initio Simulation Package (VASP).^[46] The PBE functional is employed for the exchange-correlation energy of electrons.^[31] We applied the on-site Coulomb repulsion term (U) for $3d$ transition metal oxides.^[34] Sampling of the k-points and energy cutoff for the plane-wave basis set are determined to ensure the energy convergence within 10 meV/atom and pressure convergence within 1.0 GPa. We employ the HSE06 functional for the hybrid calculation with the fraction of Fock exchange of 0.25.^[36]

4.2.2 Candidate descriptors for p-type oxides

To search a novel p-type descriptor, we use several variables including elemental information, structural properties and electronic properties. Elemental information such as electronegativity of metal element (EN_M), work function of metal element (W_M) and ionization energy of metal element (IE_M) is easily available from the CRC hand book.^[74] The oxidation states of metal elements (OS_M) are determined with the assumption that the oxidation number of oxygen is -2 . The coordination numbers of metal (oxygen) are estimated by counting the number of metal (oxygen) atoms within the cutoff length (considering the ionic radius). The electronic properties are calculated using density functional theory for instance hole effective mass (m_h), band gap ($E_{g,HSE}$) and oxygen partial weight at VBM (w_O). The calculation methods for m_h and $E_{g,HSE}$ are written in chapter 3.2.2 and chapter 3.2.3. w_O is defined as

$$w_O = \frac{\int_{VBM-0.5}^{VBM} OPDOS(\varepsilon)d\varepsilon}{\int_{VBM-0.5}^{VBM} TDOS(\varepsilon)d\varepsilon}, \quad (4.1)$$

where OPDOS and TDOS indicate the oxygen partial density of states and total density of states, respectively.

4.2.3 Pearson correlation coefficient

Pearson correlation coefficient is used to evaluate the strength of a linear correlation between two data. The coefficient has a range between -1 and $+1$. The positive (or negative) value indicates positive (or negative) linear correlation and 0 means that two data has no linear relationship. The Pearson correlation coefficient between two data (X and Y) is estimated by

$$r = \frac{\sum_{i=1}^n (X_i - \bar{X})(Y_i - \bar{Y})}{\sqrt{\sum_{i=1}^n (X_i - \bar{X})^2} \sqrt{\sum_{i=1}^n (Y_i - \bar{Y})^2}}, \quad (4.2)$$

where X_i is variable in X , \bar{X} is average of X and n is the number of variables in X . In Figure 4.1, we present various samples and their correlation coefficient. The first three figures show the extreme case where coefficients are -1 , 0 and 1 . Following two figures represent strong correlation and weak correlation.

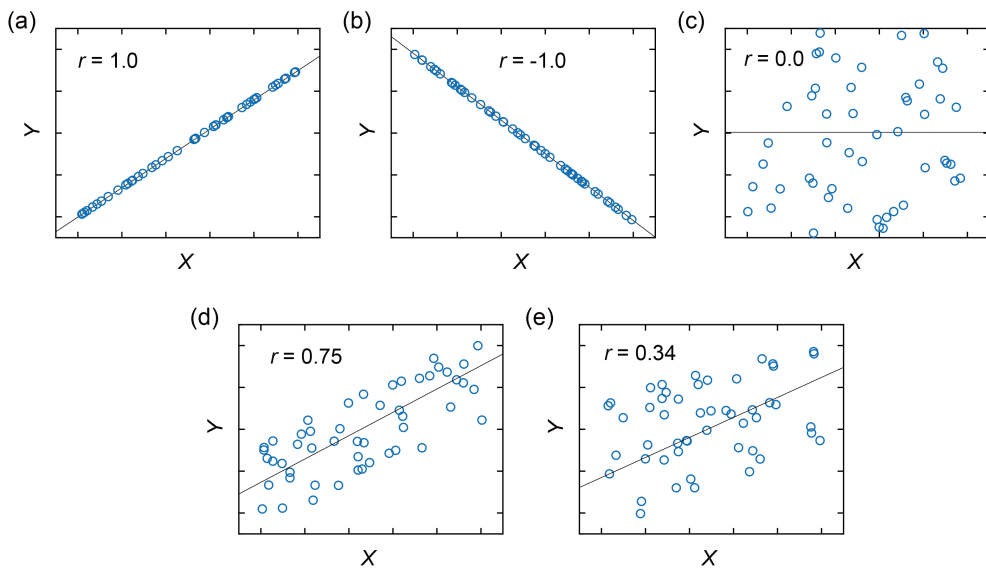


Figure 4.1 The examples of various correlation and their Pearson correlation coefficient. (a) perfect positive correlation, (b) perfect negative correlation, (c) no correlation, (d) strong positive correlation, and (e) weak positive correlation.

4.2.4 Receiver operating characteristic curve

Receiver operating character curve shows the graphical information about relationship between sensitivity and specificity for every possible cut-off. It can be used to select the most appropriate cut-off for a classification. Table 4.1 shows four conditions according to the true condition and predicted condition. The sensitivity and specificity are defined as following two equation;

$$\text{sensitivity} = \frac{\sum \text{TP}}{\sum \text{TP} + \text{FN}}, \quad (4.3)$$

$$\text{specificity} = \frac{\sum \text{TN}}{\sum \text{TN} + \text{FP}}. \quad (4.4)$$

If data points are randomly distributed regardless of the cut-off, sensitivity equals 1-specificity. If the given cut-off classify the data perfectly, both sensitivity and specificity are one.

Table 4.1 Four conditions from binary classifier

	Condition positive	Condition negative
Predicted condition positive	True positive (TP)	False positive (FP)
Predicted condition negative	False negative (FN)	True negative (TN)

4.3 Results and discussion

4.3.1 Simplified descriptor for p-type oxides

In order to find computationally efficient descriptor for p-type oxides, we estimate the correlation between FEH and various properties including hole effective mass (m_h), band gap ($E_{g,HSE}$), oxygen partial weight at VBM (w_O), electronegativity of metal element (EN_M), work function of metal element (W_M), oxidation state of metal element (OS_M), ionization energy of metal element (IE_M) and, coordination number of oxygen (CN_O) and metal element (CN_M). Figure 4.2 shows the absolute value of Pearson correlation coefficient between FEH and another property in the 43 binary compounds. There are remarkable descriptors with high correlation such as w_O , OS_M , IE_M and CN_O . To distinguish p-type oxides, however, we need to estimate the correlation in vicinity of the decision boundary at $FEH = -1$ eV. Thus, we evaluate the correlation coefficients in the 17 binary oxides with $FEH > -2$ eV. Although we restrict the data set, w_O still have high correlation as a promising descriptor. However, the other highly correlated properties from the all binary compounds are not suitable to be reliable descriptors due to their low correlation near the decision boundary. The fundamental origin of the scarcity of p-type transparent oxides is oxygen character at valence band which leads to the low valence band energy and high hole effective mass. Therefore, the low w_O is directly correlated with the p-type properties of oxides. Another reliable descriptor is $E_{g,HSE}$ of which the correlation coefficient is above 0.3 in the two data set. The

correlation can be explained by the position of valence band. In general, the valence band level goes down as the band gap widens, which results in low FEH.

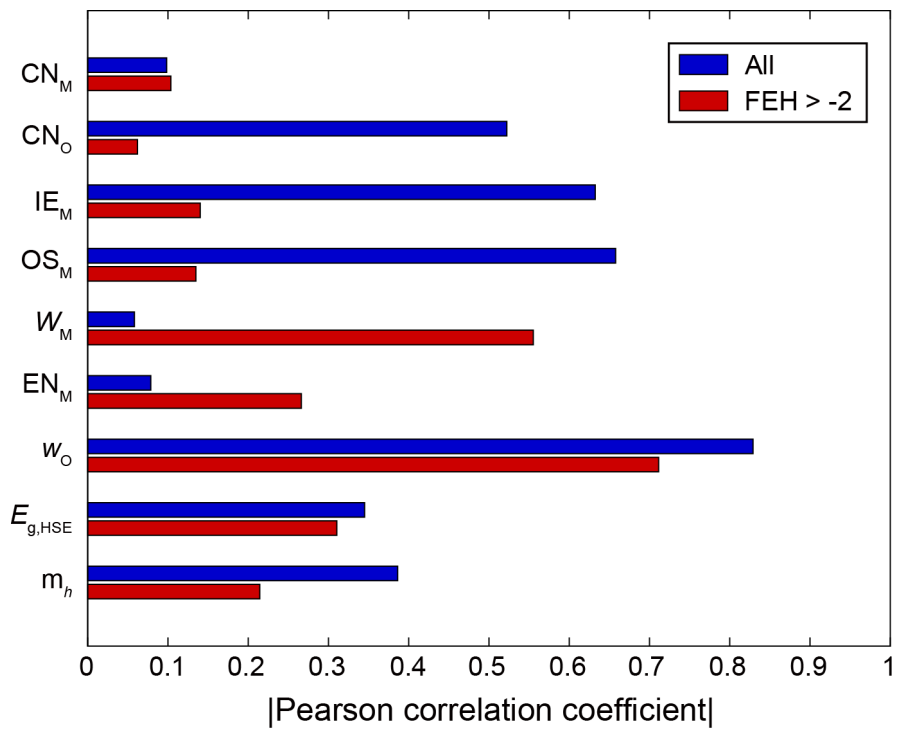


Figure 4.2 Absolute values of Pearson correlation coefficient of various factors with FEH.

The correlations of w_{O} and $E_{\text{g,HSE}}$ with FEH are observed in the extended data set including 120 ternary compounds as shown in Figure 4.3. They have negative linear correlation with FEH. The ternary compounds consist of the (number) oxides selected by design principles of p-type (Ternary_{design}), that are the Cu¹⁺ bearing and Sn²⁺ bearing oxides as well as oxychalcogenides, and randomly chosen 52 compounds (Ternary_{random}). In the Figure 4.3a, most of binary oxides and Ternary_{random} have w_{O} close to 1.0 because of the dominant contribution of oxygen 2*p* orbital to the valence band in oxides. It imply that it is almost impossible to find the oxides with high FEH without sequential procedure. Additionally, Figure 4.3a shows the previous approach using known p-type design principles succeeds in forming mixed valence band character and raising valence band level. $E_{\text{g,HSE}}$ also has linear correlation with FEH but it is weaker than the correlation between w_{O} and FEH. Additionally, it turns out that there is no p-type candidate with $E_{\text{g,HSE}} > 5$ eV.

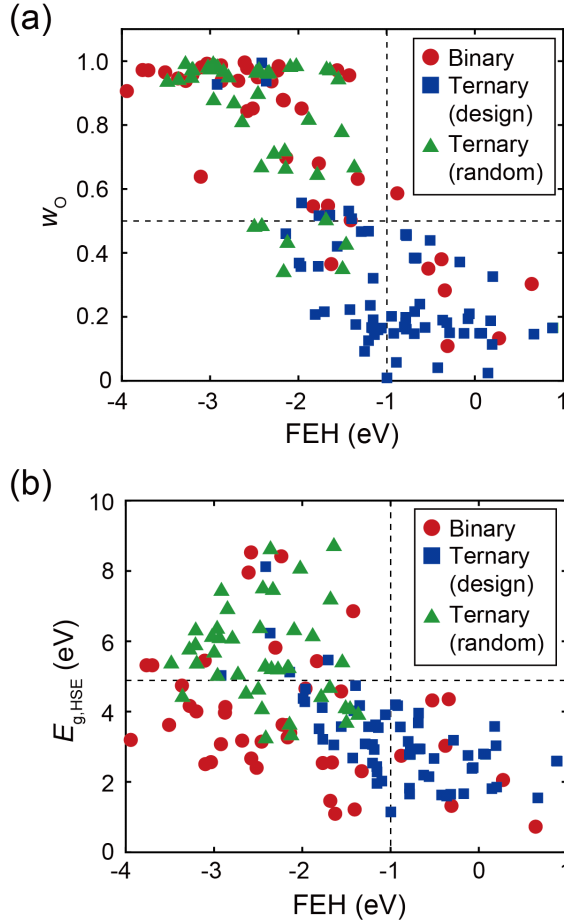


Figure 4.3 FEH versus (a) fundamental band gap ($E_{g,HSE}$) and (b) oxygen partial weight at the valence band top (w_O) for binary, ternary_{design} and ternary_{random} oxides. Vertical and horizontal dashed lines indicate the FEH and simple descriptor criteria for p-type, respectively.

The decision boundaries for w_{O} and $E_{\text{g,HSE}}$ are determined from the receiver operating characteristic (ROC) curve as illustrated in Figure 4.4. ROC curve can evaluate the power of binary classifier and detailed explanation presents in the method section (4.2.4). To estimate the ROC curve, we classify the oxides with FEH > -1 eV as positive condition and the rest as negative condition. Also, predicted positive (negative) condition in each point on the curve is defined as w_{O} or $E_{\text{g,HSE}}$ lower (higher) than decision boundary due to their negative correlation with FEH. In Figure 4.4, we notice that w_{O} is a very good descriptor since the curve is close to the left-top which indicate the perfect classification. $E_{\text{g,HSE}}$ is also quite a good descriptor. In the coarse screening step, the sensitivity is more important than the specificity because we would perform the further procedure to screen out the false positive cases. Thus, we determine the decision boundary as $w_{\text{O}} = 0.5$ and $E_{\text{g,HSE}} = 5.0$ eV where the sensitivity equals to 1.0 with the highest specificity.

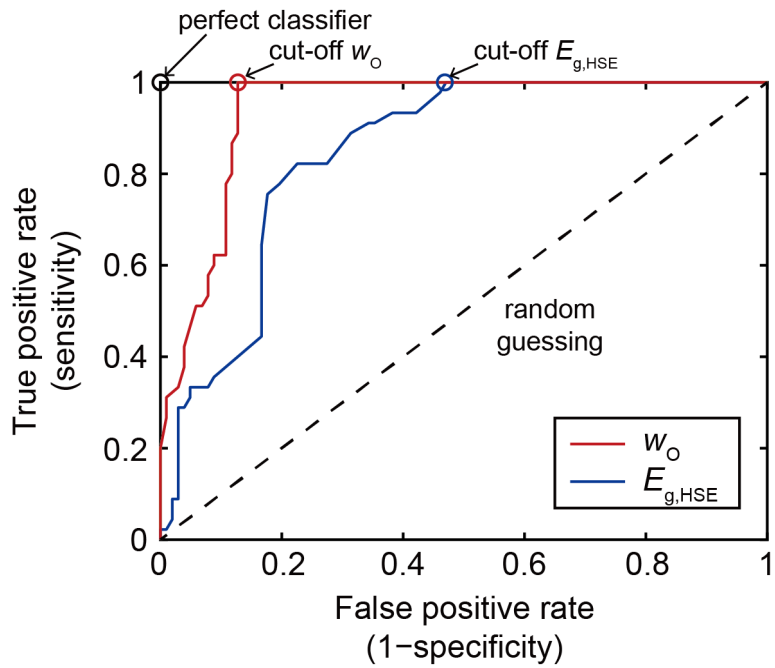


Figure 4.4 Receiver operating characteristic (ROC) curve for the w_0 and $E_{g,HSE}$. Dashed line indicates random guessing line.

4.3.2 Screening over the oxides in the AFLOW database

We use w_O and $E_{g,HSE}$ to screen all ternary and quaternary oxides in AFLOW database which includes over seventeen thousand compounds. For the efficient and effective screening, we decide the sequence according to the computational cost as shown in Figure 4.5. At the first step, we screen out unpromising materials considering the simple descriptor such as w_O and band gap. For transparency, the oxides having $E_g^{OPT} < 2.5$ eV are eliminated. In addition, we exclude the duplicated structure considering the chemical composition and space group. Since it is difficult to calculate the band gap with HSE for the entire oxides, we use band gap estimated from PBE(+ U) method for the screening. Considering the correlation between PBE and HSE band gap shown in the Figure 4.6, we convert the band gap condition from $E_{g,HSE} < 5.0$ eV and $E_{g,HSE}^{OPT} > 2.5$ eV to $E_{g,PBE} < 4.5$ eV and $E_{g,PBE}^{OPT} > 0.5$ eV. The correlation is presented in Figure 4.6. Through the procedure, we obtain about sixteen hundred compounds. In the next step, we apply the chemical filter; non-metal compounds, lanthanides and actinides (except for La & Ac) as well as halogen and polyanion compounds are excluded. The halogen and poly-anion compounds give the lower FEH value rather than oxide counterpart due to their more stable bonding. Additionally, we do not consider the $3d$ transition metal bearing oxides from vanadium to nickel because $d-d$ transition of transition metal oxide can reduce the transparency. Through the above procedure, we cut the searching space to 279 oxides. We perform the HSE calculation for the survived compounds and only 105 oxides satisfy two band gap

conditions; the transparency ($E_{\text{g,HSE}}^{\text{OPT}} > 2.5 \text{ eV}$) and $E_{\text{g,HSE}} < 5.0 \text{ eV}$. Finally, we evaluate the FEH and only 47 compounds satisfy the condition of $\text{FEH} > -1 \text{ eV}$. The survived candidates are listed in Table 4.2.

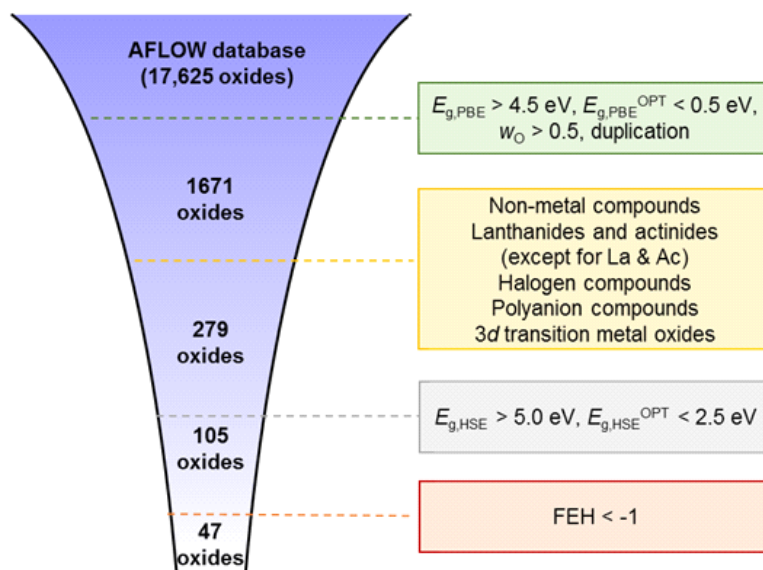


Figure 4.5 Screening procedure for discovery of p-type transparent semiconducting oxides.

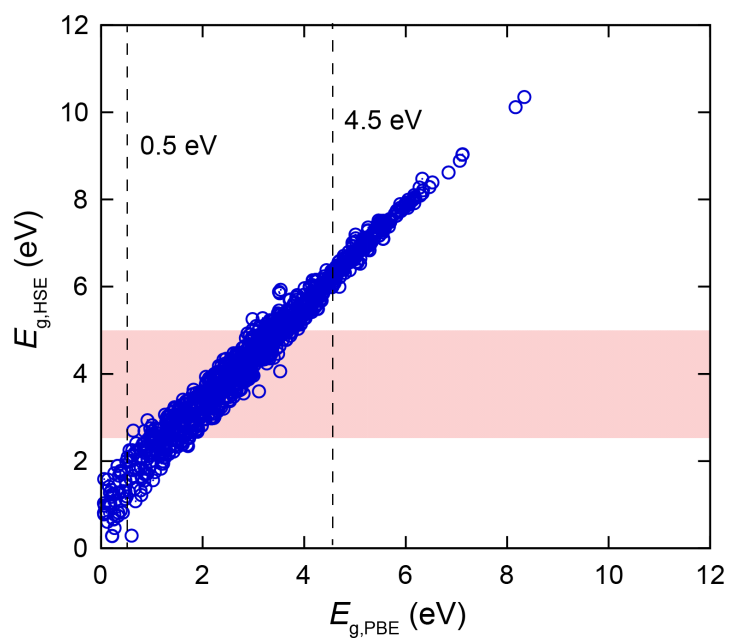


Figure 4.6 Comparison with PBE band gap and HSE band gap. Red shadow represents the cut-off range of $E_{g,HSE}$. Two dashed lines indicate the minimum and maximum $E_{g,PBE}$ corresponding to the $E_{g,HSE}$.

Table 4.2 p-type candidates satisfying $FEH > -1$ eV and $E_{g,HSE}^{opt} > 2.5$ eV. The hole effective mass are also provided. (m_1 , m_2 , m_3) are effective masses along the principal axis and m_{avg} is the harmonic average of them.

Name	ICSD index	FEH	hole effective mass		$E_{g,HSE}^{opt}$
			m_{avg}	(m_1, m_2, m_3)	
SnO	15516	0.65	1.25	(2.08,2.08,0.69)	2.79
Rh ₂ O ₃	33645	-0.41	3.21	(1.69,5.92,5.80)	2.70
SnO	20624	-0.92	0.99	(3.81,1.05,0.56)	2.70
CuLiO	40156	0.88	2.77	(2.59,2.59,3.22)	3.10
Na ₂ PtO ₂	25018	0.21	2.64	(1.09,9.76,8.67)	3.32
La ₂ O ₂ Te	27004	0.20	0.65	(1.05,0.31,2.25)	3.12
CuAlO ₂	25593	0.18	2.73	(5.26,2.27,2.13)	4.15
CuAlO ₂	95661	0.18	3.64	(3.11,2.87,6.49)	3.58
CuNaO	15099	0.08	9.01	(18.4,18.4,4.46)	2.96
CuRhO ₂	29214	0.06	2.23	(5.57,1.77,1.65)	3.02
Li ₂ PdO ₂	61199	-0.02	2.49	(5.57,1.41,3.12)	3.85
La ₂ O ₂ S ₂	68498	-0.06	0.86	(90.6,0.58,0.57)	3.12
CuGaO ₂	95664	-0.06	3.41	(3.24,2.37,6.68)	3.78
CuGaO ₂	188625	-0.08	2.26	(1.52,2.25,4.44)	4.04
La ₂ O ₂ S ₂	2455	-0.10	0.86	(0.58,0.57,116)	3.21
BaCu ₂ O ₂	9456	-0.12	2.34	(4.96,4.96,1.14)	2.75
AuScO ₂	95669	-0.28	0.79	(0.41,0.88,3.69)	2.98
NaRhO ₂	66280	-0.28	6.25	(5.02,4.03,31.0)	3.39
CuInO ₂	95670	-0.32	3.10	(2.48,2.19,9.39)	2.62
CuInO ₂	91855	-0.36	2.62	(1.80,2.08,9.09)	2.85

Name	ICSD index	FEH	hole effective mass		$E_{g,HSE}^{opt}$
			m_{avg}	(m_1, m_2, m_3)	
MgRh ₂ O ₄	109299	-0.48	8.12	(7.94,8.21,8.21)	3.11
Cu ₂ NaO ₂	169713	-0.51	2.19	(9.11,157,0.80)	2.83
ZnRh ₂ O ₄	109298	-0.53	4.55	(4.40,4.63,4.63)	2.91
Cu ₂ LiO ₂	69051	-0.62	2.06	(43.5,1.40,1.40)	2.79
Sc ₂ O ₂ S	2450	-0.64	1.00	(0.69,0.73,6.01)	3.83
CaRh ₂ O ₄	170597	-0.66	11.17	(27.6,30.6,5.01)	2.79
CuScO ₂	151929	-0.68	4.35	(3.71,2.77,16.84)	3.78
CuScO ₂	65547	-0.69	2.65	(6.63,1.94,2.15)	3.70
CuKO	25695	-0.69	5.67	(17.6,17.6,2.41)	2.99
CuReO ₄	416510	-0.75	-	-	2.71
CuRbO	15100	-0.78	6.04	(399,399,2.04)	2.81
SrCu ₂ O ₂	25002	-0.80	1.58	(1.17,1.17,5.37)	3.15
Y ₂ OS ₂	67503	-0.89	1.49	(3.14,2.88,0.75)	3.67
CuYO ₂	60848	-0.92	3.21	(2.08,12.6,2.68)	4.06
CuYO ₂	35580	-0.94	3.97	(2.99,2.62,24.8)	4.48
LiRhO ₂	59179	-0.97	16.95	(14.2,19.4,18.2)	3.51
Ba ₃ BPO ₃	402017	0.42	0.80	(5.33,4.20,0.30)	2.51
Sr ₃ BPO ₃	401207	0.14	1.15	(16.0,10.2,0.41)	3.27
LaCuOSe	96758	-0.02	0.78	(0.59,0.59,1.99)	2.84
La ₂ SiO ₄ Se	59941	-0.15	1.07	(10.8,0.37,136)	3.82
LaCuOS	86249	-0.30	1.02	(0.78,0.78,2.52)	3.02
AgCNO	18149	-0.56	1.53	(1.07,6.85,1.14)	4.70
K ₃ Sb ₇ O ₉ S ₃	4215	-0.70	5.37	(259,42.1,1.88)	2.53
In ₆ PtGe ₂ O ₉	170897	-0.91	3.12	(3.28,3.24,2.88)	2.87

Name	ICSD index	FEH	hole effective mass		$E_{g,HSE}^{opt}$
			m_{avg}	(m_1, m_2, m_3)	
Ta ₂ Li ₁₆ ON ₈	71696	-0.99	6.18	(4.87, 7.06, 7.25)	4.66
Nb ₂ Li ₁₆ ON ₈	82635	-0.99	5.91	(3.92, 8.04, 7.78)	4.62
Nb ₂ Li ₁₆ ON ₈	174443	-0.99	5.95	(4.03, 7.91, 7.70)	4.63

Figure 4.7 shows the FEH values and hole effective mass of the 105 oxides satisfying the hybrid band gap conditions. The transparency of each data point is determined by $E_{g,HSE}^{OPT}$; the symbol is completely transparent for $E_{g,HSE}^{OPT} > 3.1$ eV and it becomes progressively opaque down to $E_{g,HSE}^{OPT} = 1.8$ eV. The survived oxides can be categorized as three groups such as Cu and Pt group bearing oxides as well as multi-anion compounds. It is widely known that $3d$ orbital of Cu^{1+} at the valence band results in the high valence band position and p-type conductivity.^[63] However, since Cu^{1+} bearing oxides were discussed in the previous chapter, we do not conduct further discussion in this part. Pt group (Pt^{2+} , Pd^{2+} and Rh^{3+}) bearing oxides have similar valence band character to the Cu^{1+} bearing oxides that the hybridization of metal d and oxygen $2p$ orbitals forms valence band top. However, they have high hole effective mass due to localized metal d character in valence band. Multi-anion compounds can be promising p-type oxides since another anion increases the valence band level and reduces hole effective mass due to larger orbital size than O. In the case of SnO, the hybridization of metal s character and oxygen p orbital at the valence band leads to the higher valence band level and low hole effective mass. However, we does not discover the oxides of which valence band consists of metal s orbital except for the SnO. The oxides composed by metal s and oxygen $2p$ orbitals such as Sn^{2+} , Pb^{2+} and Bi^{3+} bearing oxides have small band gap. Thus, most of them do not satisfy the transparency condition and do not survive to the last.

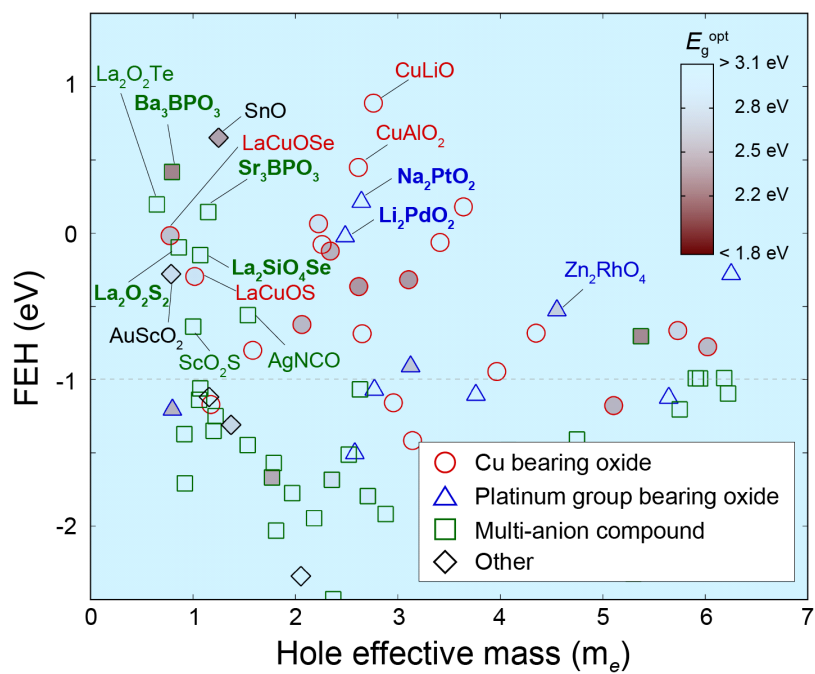


Figure 4.7 FEH and hole effective mass for 105 oxides of which $E_{g,HSE}^{opt}$ is higher than 2.5 eV and $E_{g,HSE}$ is lower than 5.0 eV. The transparency of each material represents the optical band gap.

4.3.3 Promising candidates

Although there is no candidate surpass the $\text{La}_2\text{O}_2\text{Te}$ proposed in the chapter 3, Figure 4.7 reveals several notable and unreported candidates as far as we are aware, such as Na_2PtO_2 , $\text{La}_2\text{O}_2\text{S}_2$, Sr_3BPO_3 , Ba_3BPO_3 and $\text{La}_2\text{SiO}_4\text{Se}$. The Pt group bearing oxides can be classify the two groups; one is Rh^{3+} bearing oxides, the other is Pt^{2+} and Pd^{2+} bearing oxides. It is widely known that Rh^{3+} bearing oxides with spinel configuration for example ZnRh_2O_4 have p-type conductivity. The Rh^{3+} builds low-spin octahedral complexes of d^6 configuration^[18] as shown in Figure 4.8a. The splitting between occupied t_{2g} state and unoccupied e_g state lead to the band gap and occupied t_{2g} state gives similar valence band character to the d^{10} configuration of Cu^{1+} . Thus, the class of d^6 octahedral transition metal oxides (NaRhO_2 and LiRhO_2), not just spinel configuration, has high FEH. However, they have high hole effective mass due to localized d state at the valence band.

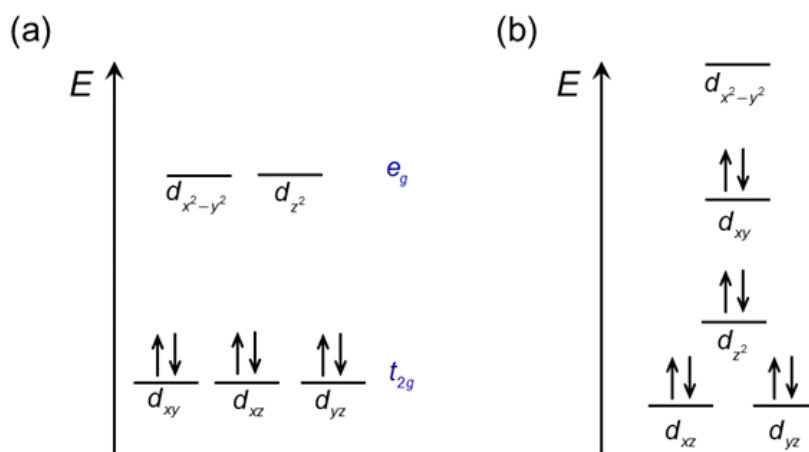


Figure 4.8 Splitting diagram of the d orbital electrons in (a) a low-spin octahedral and (b) a square planar ligand field. The arrow in each level indicates an occupied electron.

The Pd²⁺ or Pt²⁺ bearing oxides have been less studied than the Rh³⁺ bearing oxides. However, it is known that Pd²⁺ bearing oxides such as PdO exhibits p-type behavior.^[75] The square planar complex of d^8 configuration gives similar valence band character to the d^{10} configuration of Cu¹⁺ and d^6 configuration of Rh³⁺ which is fully occupied d_{z^2} state at the valence band top. The Na₂PtO₂ and Li₂PdO₂ have square planar complex, which results in the high FEH with 0.21 eV and -0.02 eV, respectively. Figure 4.9 exhibits the crystal structure, electronic structure and the defect formation energies of Na₂PtO₂ with higher FEH. The hybridization of Pt-5*d* and O-2*p* states in valence band leads to the high FEH. Also, it has anisotropic m_h since Pt atoms are placed along the one direction. The harmonic averaged m_h (2.64 m_e) is almost same to that of CuAlO₂ (2.66 m_e). Along the Pt atoms, however, it shows low m_h (1.09 m_e), which can enhance the hole mobility. From the defect calculation, we find that Na_{Pt} and V_{Pt-H} can be the intrinsic acceptor. However, their calculated transition level of (0/-) are 0.73 eV and 1.13 eV above VBM, which are deeper than Cu vacancies in known p-type oxides (0.4 to 0.7 eV). Thus, we try to find dopants to form shallower acceptors. Li substitutional defects at Pt sites are more shallow acceptor of which (0/-) transition level is 0.59 eV. However, doping could be difficult due to its higher defect formation energy. Li₂PdO₂ has similar crystal and electron structure to Na₂PtO₂ and therefore, it has high FEH. Another M^I₂M^{II}O₂ (M^I=alkali metal, M^{II}=Pd, Pt) structure, K₂PdO₂, also has square planar complex and satisfy p-type condition (FEH =

-0.62 eV) even though it is not listed as final candidates. By passing, $\text{In}_6\text{PtGe}_2\text{O}_9$ also has FEH above -1.0 eV because Pt ions act as anions by receiving electrons.

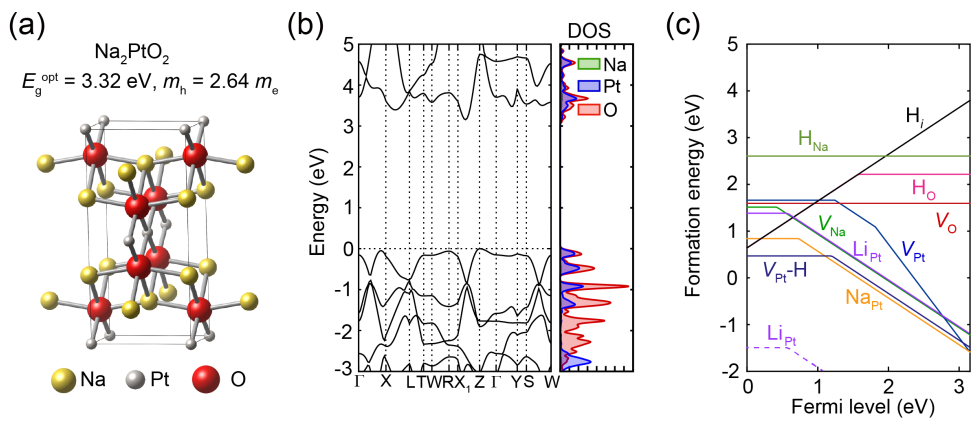


Figure 4.9 (a) The atomic structure of Na_2PtO_2 . (b) Band diagram and partial density of states using gap correction with HSE scheme. (c) The defect formation energy diagram at the oxygen-rich condition.

Most of good candidates with high FEH and low effective mass are multi-anion compounds including layered oxychalcogenides. In the ternary compounds, $\text{La}_2\text{O}_2\text{Te}$ catch the eye but it was proposed in the previous chapter. Following ternary candidate is $\text{La}_2\text{O}_2\text{S}_2$ which has comparable FEH and m_h with LaCuOSe known as highest conductivity. The structure consists of O and S layer in Figure 4.9a, which results in the anisotropic hole effective mass. Since S-2p orbital mainly contributes the valence band top as shown in Figure 4.9b, the conduction of hole is expected to be dominant in the planar directions on the S layer. The defect formation energies in Figure 4.9c shows that $\text{La}_2\text{O}_2\text{S}_2$ would behave as p-type in the oxygen-rich condition. There is no intrinsic defect to generate hole. However, $\text{Ca}_{\text{La}}^{1-}$ would be a good source of holes since it behaves a shallow acceptor and its formation energy is lower than hole compensated defects such as H_i^+ .

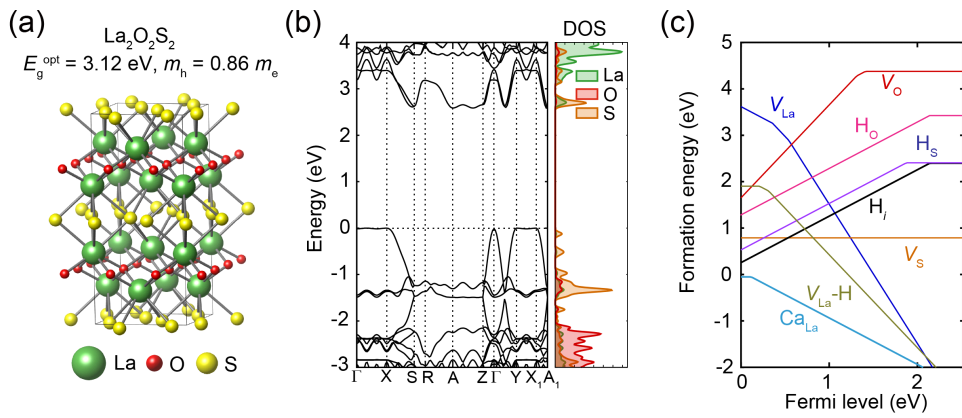


Figure 4.10 (a) The atomic structure of $\text{La}_2\text{O}_2\text{S}_2$. (b) Band diagram and partial density of states using gap correction with HSE scheme. (c) The defect formation energy diagram at the oxygen-rich condition.

$\text{La}_2\text{SiO}_4\text{Se}$ is another layered oxychalcogenide compound with high FEH (-0.15 eV), low m_h ($1.07 m_e$) and wide band gap (3.82 eV). In Figure 4.11a, Se atoms are located only in certain layers, which results in the anisotropic hole effective mass. The dominant Se-4p states at the valence band top raises the valence band level and reduces hole effective mass in planar direction as shown in Figure 4.11b. From the defect formation energies in Figure 4.12c, it is confirmed that it can be intrinsic p-type materials. V_{La} with two hydrogen defects can be a source of holes. Additionally, Ca doping at the La sites can be a promising hole source.

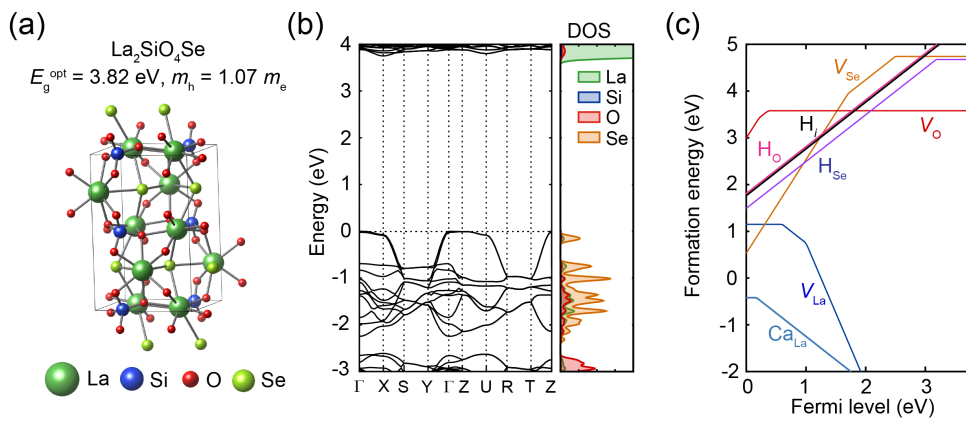


Figure 4.11 (a) The atomic structure of $\text{La}_2\text{SiO}_4\text{Se}$. (b) Band diagram and partial density of states using gap correction with HSE scheme. (c) The defect formation energy diagram at the oxygen-rich condition.

Oxychalcogenides are considered as promising p-type candidates since p orbital of chalcogen atoms is more dispersive than O- $2p$ orbital. In this aspect, multi-anion compounds including nitrogen or phosphorus can exhibit the p-type conductivity. $M^{II}_3BPO_3$ ($M^{II}=\text{Sr, Ba}$) are notable candidates in this class. Sr_3BPO_3 has high FEH (0.14 eV) and low hole effective mass ($1.15 m_e$). Figure 4.12a-b shows the atomic and electronic structures of Sr_3BPO_3 . The layered structure results in the anisotropic m_h which is lower in the normal direction ($0.41 m_e$) than in the lateral direction. Strong overlap between Sr- $5s$ and P- $3p$ states enhance the mobility in the normal direction. We also propose Ba_3BPO_3 as a p-type candidate due to its high FEH (0.42 eV) and low m_h ($0.80 m_e$) in spite of its low band gap (2.51 eV). It has almost identical configurational and electronic structure to Sr_3BPO_3 as illustrated in Figure 4.13a-b. Since Ba- $6s$ orbital at the valence band top is larger than Sr- $5s$, it is expected that the conductivity of Ba_3BPO_3 is better than Sr_3BPO_3 . In spite of their high FEH and low m_h , there are no intrinsic source of holes as shown in Figure 4.12c and Figure 4.13c, which are estimated from PBE calculation.

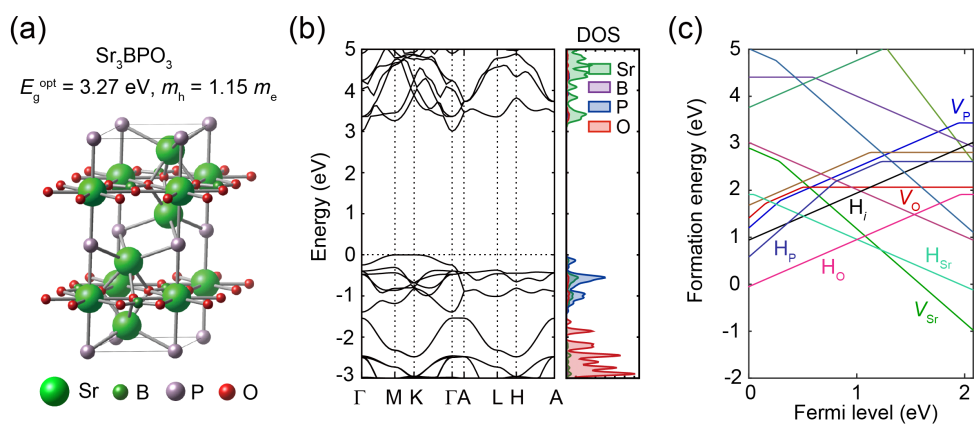


Figure 4.12 (a) The atomic structure of Sr_3BPO_3 . (b) Band diagram and partial density of states using gap correction with HSE scheme. (c) The defect formation energy diagram at the oxygen-rich condition with PBE scheme.

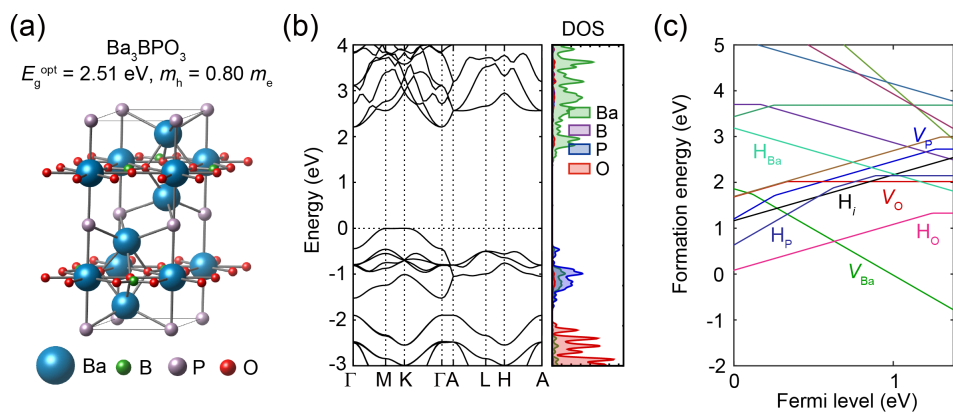


Figure 4.13 (a) The atomic structure of Ba_3BPO_3 . (b) Band diagram and partial density of states using gap correction with HSE scheme. (c) The defect formation energy diagram at the oxygen-rich condition with PBE scheme.

4.4 Summary

In this study, we introduce a high-throughput protocol to discovery new p-type oxide semiconductors. We evaluate the correlation of FEH with the elemental information and the factors deposited in the material database. Then, we identify two efficient and highly correlated descriptors such as oxygen partial weight at VBM and fundamental band gap. Next, high-throughput screening calculation was performed on the 17,625 oxides deposited in the AFLOW database. We identify several p-type candidates including Na_2PtO_2 , $\text{La}_2\text{O}_2\text{S}_2$ and $\text{La}_2\text{SiO}_4\text{Se}$. We expect that proposed materials would be realized through the further experiment.

Chapter 5

Conclusion

In this dissertation, we searched novel p-type transparent semiconducting oxides through the high-throughput screening based on the density functional theory. Since the descriptors in the previous studies such as hole effective mass and branch point energy have a limitation to distinguish the known n-type and p-type oxides, we focused on finding efficient and reliable descriptors by considering the defect chemistry. As a result, we succeeded to identify a promising descriptor for p-type oxides called as FEH. Additionally, we described the fundamental reason why FEH can be a promising p-type descriptor. Through the high-throughput screening considering the hydrogen descriptor, we proposed new p-type candidates such as $\text{La}_2\text{O}_2\text{Te}$ and CuLiO . Their p-type behaviors can be explained by the hybridized orbital characters at the valence band top. Also, we showed the source of holes through the defect formation energy calculation.

Next, we extended the screening space to most of oxides (~17,000 compounds) deposited in the Aflow database. To enhance the screening speed, we built a multi-step procedure consisting of fast step and accurate step. For the fast step, we proposed new descriptors, oxygen partial weight at valence band top and fundamental band gap, which can be rapidly estimated and are highly

correlated with FEH. Through the multi-step high-throughput screening, we identified new class of p-type transparent oxide semiconductors including Na_2PtO_2 , $\text{La}_2\text{O}_2\text{S}_2$ and $\text{La}_2\text{SiO}_4\text{Se}$. Additionally, we evaluated the intrinsic and hydrogen related defect formation energy calculation to identify the source of holes.

As a result, we proposed several p-type candidates through the high-throughput screening. We expect that the suggested p-type candidate can be validated in experiment. Also, this study can contribute to realizing the highly efficient transparent electronic devices.

Bibliography

- [1] Fortunato, E., Barquinha, P. & Martins, R. *Adv. Mater.* **24**, 2945-2986 (2012).
- [2] Cui, J. *et al.* *Adv. Mater.* **13**, 1476-1480 (2001).
- [3] Varghese, O. K., Paulose, M. & Grimes, C. A. *Nat. Nanotech.* **4**, 592-597 (2009).
- [4] Klasens, H. A. & Koelmans, H. *Solid-State Electron.* **7**, 701 (1964).
- [5] Boesen, G. F. & Jacobs, J. E. *Proc. IEEE* **26**, 2094 (1968).
- [6] Nomura, K., Ohta, H., Ueda, K., Kamiya, T., Hirano, M., & Hosono, H. *Science* **300**, 1269-1272 (2003).
- [7] Prins, M. W. J., Grosse-Holz, K. O., Müller, G., Cillessen, J. F. M., Giesbers, J. B., Weening, R. P., & Wolf, R. M. *Appl. Phys. Lett.*, **68**, 3650-3652 (1996).
- [8] Prins, M. W. J., Zinnemers, S. E., Cillessen, J. F. M., & Giesbers, J. B. *Appl. Phys. Lett.*, **70**, 458-460 (1997).
- [9] Nomura, K., Ohta, H., Takagi, A., Kamiya, T., Hirano, M., & Hosono, H. *Nature*, **432**, 488 (2004).
- [10] Tiedje, T., Wronski, C. R., Abeles, B., & Cebulka, J. M. *Solar Cells*, **2**, 301-318 (1980)..
- [11] Kawazoe, H. *et al.* *Nature* **389**, 939-942 (1997).
- [12] Nagarajan, R. *et al.* *Int. J. Inorg. Mater.* **3**, 265-270 (2001)
- [13] Tate, J. *et al.* *Thin Solid Films* **411**, 119-124 (2002).

- [14] Marquardt, M. A., Ashmore, N. A. & Cann, D. P. *Thin Solid Films* **496**, 146–156 (2006).
- [15] Sheets, W. C. *et al. Inorg. Chem.* **47**, 2696–2705 (2008).
- [16] Kudo, A., Yanagi, H., Hosono, H. & Kawazoe, H. *Appl. Phys. Lett.* **73**, 220–222 (1998).
- [17] Ueda, K. & Hosono, H. *J. Appl. Phys.* **91**, 4768–4770 (2002).
- [18] Mizoguchi, H. *et al. Appl. Phys. Lett.* **80**, 1207–1209 (2002).
- [19] Wager, J. F., Kezler, D. A. & Presley, R. E. *Transparent Electronics* 1st edn (Springer, 2008)
- [20] Caraveo-Frescas, J. A. *et al. ACS Nano* **7**, 5160–5167 (2013).
- [21] Engel, C. J., Polson, T. A., Spado, J. R., Bell, J. M. & Fillinger, A. *J. Electrochem. Soc.* **155**, F37–F42 (2008).
- [22] Hautier, G., Miglio, A., Ceder, G., Rignanese, G.-M. & Gonze, X. *Nat. Comm.* **4**, 2292 (2013).
- [23] Bhatia, A. *et al. Chem. Mater.* **28**, 30–34 (2016).
- [24] Sarmadian, N., Saniz, R., Partoens, B. & Lamoen, D. *Sci. Rep.* **6**, 20446 (2016).
- [25] Cerqueira, T. F. T., Lin, S., Amsler, M., Goedecker, S., Botti, S., & Marques, M. A. L. *Chem. Mater.* **27**, 4562–4573 (2015).
- [26] Yim, K., Youn, Y., Lee, M., Yoo, D., Lee, J., Cho, S. H., & Han, S. *npj Comp. Mater.* **4**, 17 (2018).
- [27] Hohenberg, P. & Kohn, W. *Phys. Rev.* **136**, B864 (1964)
- [28] Kohn, W. and Sham, L. J. *Phys. Rev.* **140**, A1133 (1965)
- [29] Perdew, J. P. & Yue, W. *Phys. Rev. B* **33**, 8800 (1986).
- [30] Becke, A. D. *Phys. Rev. A* **38**, 3098 (1988).

- [31] Perdew, J. P., Emzerhog, M., & Burke, K. *Phys. Rev. Lett.* **77**, 3865 (1996).
- [32] Hybertsen, M. S., Schlter, M., & Christensen, N. E. *Phys. Rev. B* **39**, 9028–9041 (1989).
- [33] Anisimov, V., Aryasetiawan, F., & Lichtenstein, A. I. *J. Phys. Condens. Matter* **9**, 767–808 (1997).
- [34] Wang, L., Maxisch, T. & Ceder, G. *Phys. Rev. B* **73**, 195107 (2006).
- [35] Hedin, L. *Phys. Rev.* **139**, A796 (1965).
- [36] Heyd, J., Scuseria, G. E. & Ernzerhof, M. *J. Chem. Phys.* **118**, 8207-8215 (2003).
- [37] Krukau, A. V. *et al. J. Chem. Phys.* **125**, 224106 (2006).
- [38] Perdew, J. P., Emzerhog, M. & Burke, K. *J. Chem. Phys.* **105**, 9982 (1996).
- [39] Kumagai, Y. & Oba, F. *Phys. Rev. B*, **89**, 195205 (2014).
- [40] Lany, S. & Zunger, A. *Phys. Rev. Lett.* **98**, 045501 (2007).
- [41] Van de Walle, C. G. & Neugebauer, J. *J. Appl. Phys.* **95**, 3851-3879 (2004).
- [42] Lany, S. & Zunger, A. *Modell. Simul. Mater. Sci. Eng.* **17**, 084002 (2009).
- [43] Makov, G. & Payne, M. C. *Phys. Rev. B* **51**, 4014–4022 (1995).
- [44] Freysoldt, C., Neugebauer, J. & Van de Walle, C. G. *Phys. Rev. Lett.* **102**, 16402 (2009).
- [45] Lany, S. & Zunger, A. *Phys. Rev. B* **78**, 235104 (2008).
- [46] Kresse, G. & Hafner, J. Ab initio molecular dynamics for liquid metals. *Phys. Rev. B* **47**, 558 (1993).

- [47] Park, S., Lee, B., Jeon, S. H. & Han, S. *Curr. Appl. Phys.* **11**, s337–s340 (2011).
- [48] Yim, K. *et al. NPG Asia Mater.* **7**, e190 (2015).
- [49] Schleife, A., Fuchs, F., Rödl, C., Furthmüller, J. & Bechstedt, F. *Appl. Phys. Lett.* **94**, 012104 (2009).
- [50] Katayama, S., Hayashi, H., Kumagai, Y., Oba, F. & Tanaka, I. *J. Phys. Chem. C* **120**, 9604–9611 (2016).
- [51] Van De Walle, C. G. *Phys. Rev. Lett.* **85**, 1012–1015 (2000).
- [52] Kang, Y. *et al. Adv. Electron. Mater.* **1**, 1400006 (2015).
- [53] Lyons, J. L., Janotti, A. & Van de Walle, C. G. *Appl. Phys. Lett.* **95**, 252105 (2009).
- [54] Reynolds, J. G. *et al. Appl. Phys. Lett.* **102**, 152114 (2013).
- [55] Stevanović, V., Lany, S., Ginley, D. S., Tumas, W. & Zunger, A. *Phys. Chem. Chem. Phys.* **16**, 3706–14 (2014).
- [56] Robertson, J. *J. Vac. Sci. Technol. B* **18**, 1785 (2000).
- [57] Xiong, K., Robertson, J. & Clark, S. J. *J. Appl. Phys.* **102**, 83710 (2007).
- [58] Pelatt, B. D., Ravichandran, R., Wager, J. F. & Keszler, D. A. *J. Am. Chem. Soc.* **133**, 16852–16860 (2011).
- [59] Van de Walle, C. G. & Neugebauer, J. *Nature* **423**, 626–8 (2003).
- [60] FIZ Karlsruhe, Inorganic Crystal Structure Database, available at: <http://icsd.fiz-karlsruhe.de>.
- [61] Alkauskas, A., Broqvist, P. & Pasquarello, A. *Phys. Rev. Lett.* **101**, 046405 (2008).
- [62] Quackenbush, N. F. *et al. Chem. Mater.* **25**, 3114–3123 (2013).

- [63] Raebiger, H., Lany, S. & Zunger, A. *Phys. Rev. B* **76**, 045209 (2007).
- [64] Scanlon, D. O., Buckeridge, J., Catlow, C. R. A. & Watson, G. W. *J. Mater. Chem. C* **2**, 3429 (2014).
- [65] Scanlon, D. O., Morgan, B. J. & Watson, G. W. *J. Chem. Phys.* **131**, 124703 (2009).
- [66] Huang, D. & Pan, Y. *Can. J. Phys.* **88**, 927–932. (2010).
- [67] Yim, K. *et al. Sci. rep.* **7**, 40907 (2017).
- [68] Yan, Q. *et al. Proc. Natl. Acad. Sci.* **114**, 3040–3043 (2017).
- [69] Curtarolo, S. *et al. Nat. Mater.* **12**, 191–201 (2013).
- [70] Yang, J., Sudik, A., Wolverton, C. & Siegel, D. J. *Chem. Soc. Rev.* **39**, 656–675 (2010).
- [71] Curtarolo, S. *et al. Comput. Mater. Sci.* **58**, 227–235 (2012).
- [72] Jain, A. *et al. APL Mater.* **1**, 011002 (2013).
- [73] Saal, J. E., Kirklin, S., Aykol, M., Meredig, B. & Wolverton, C. *JOM* **65**, 1501–1509 (2013).
- [74] Lide, D. R. *CRC Handbook of Chemistry and Physics* (CRC Press, 2005).
- [75] Dare-Edwards, M. P., Goodenough, J. B., Hamnett, A. & Katty, A. *Mat. Res. Bull.* **19**, 435-442 (1984).

국문초록

투명 산화물 반도체는 디스플레이나 태양전지 패널 등에 다양하게 이용되고 있다. 특히 In_2O_3 나 ITO와 같은 n형 산화물 반도체의 개발은 투명한 전자기기를 가능하게 하였다. 높은 효율의 투명 전자기기를 개발하기 위해서는 n형 산화물과 비견될 정도로 우수한 p형 투명 산화물 반도체 소자가 필요하다. 그러나 우수한 성능의 p형 산화물 반도체를 찾기 위한 막대한 노력에도 불구하고, 실제 기기에 사용할 수 있을 정도의 성능을 지니는 p형 반도체는 없다고 말할 수 있을 정도이다. 최근 새로운 p형 산화물 반도체를 찾기 위한 제일원리계산 기반의 고속 전산 스크리닝 연구가 진행되었고 이를 통해 기존에 알려지지 않은 새로운 후보 물질들을 제한하였다. 하지만 제안된 물질 중 어느 것도 p형 전도 특성의 실험 검증이 이루어지지 않았다. 이는 기존 스크리닝 연구의 한계로 더 나은 선별자의 필요성을 보여준다.

본 연구에서는 수소 침입형 결함의 형성에너지를 사용하여 양공(hole)의 농도와 관련된 높은 정확도와 빠른 계산 속도를 가지는 새로운 선별자를 제안하였다. 새롭게 제안한 수소 선별자의 예측력은 이 선별자가 기존의 알려진 p형, n형 산화물 반도체를 성공적으로 구별하는 것을 통하여 확인하였다. 이 수소 선별자를 활용하여 이성분계 산화물과 일부 삼성분계 물질에 대해서 고속 전산 스크리닝 계산을 진행하였다. 이 때 삼성분계 물질은 기존 p형 산화물들의 특성을 바탕으로 Sn^{2+} 나 Cu^{1+} 가 포함된 산화물이나 옥

시칼코게나이드 (oxychalcogenides) 물질로 한정하였다. 이러한 연구를 통하여 $\text{La}_2\text{O}_2\text{Te}$ 와 CuLiO 를 새로운 p형 산화물 후보군으로 제안하였다. 또한 모든 내제결합들의 결합 형성 에너지를 분석하여 양공을 형성할 수 있는 결합을 찾았다. 추가적으로, 수소 선별자와 쉽게 계산할 수 있는 인자들 사이의 상관관계를 분석하였고 이를 통해 효율적인 새로운 선별자를 찾았다. 이렇게 찾은 선별자와 기존 수소 선별자를 이용한 다단계 고속 전산 스크리닝 방법을 제안하였고 이를 통해 Aflow 데이터베이스에서 제공하는 대부분의 산화물들 (약 17,000 여개) 에 대한 분석을 진행하였다. 이러한 연구를 통해 최종적으로 Na_2PtO_2 , $\text{La}_2\text{O}_2\text{S}_2$, $\text{La}_2\text{SiO}_4\text{Se}$ 라는 새로운 p형 산화물 반도체 후보군을 제안하였다.

주요어: 범밀도함수, 고속 대량 선별 계산, p형 투명산화물 반도체
학 번: 2014-30231